Electronic Supplementary Information

Chiral bifacial indacenodithiophene-based π-conjugated polymer with chirality-induced spin selectivity

Shuang Li,[a] Fumitaka Ishiwari,*[a,b,c,d] Scott Zorn,[a] Kazuharu Murotani,[a] Mikhail Pylnev,[a] Koji Taniguchi,[e,c] and Akinori Saeki[a,d]

*To whom correspondence should be addressed.
E-mail: ishiwari@chem.eng.osaka-u.ac.jp (F.I.)

Table of Contents

1. Materials. Unless otherwise stated, all commercial reagents were used as received. Compounds **3**[S1] and **5**[S2] were prepared according to previously reported procedures and unambiguously characterized by NMR spectroscopy. HOPG

2. General. NMR spectroscopy measurements in solution were carried out on a Bruker AVANCE-III spectrometer (600 MHz for ^{1}H and 150 MHz for ^{13}C) or JEOL JNM-ECS400 (400 MHz for ^{1}H and 100 MHz for ^{13}C). Chemical shifts (δ) are expressed relative to the resonances of the residual non-deuterated solvents for ^{1}H [$CDCl_3$: ^{1}H(δ) = 7.26 ppm] and ^{13}C [$CDCl_3$: ^{13}C(δ) = 77.16 ppm]. Absolute values of the coupling constants are given in Hertz (Hz), regardless of their sign. Multiplicities are abbreviated as singlet (s), doublet (d), triplet (t) and multiplet (m). Infrared (IR) spectra were recorded at 25 °C on a JASCO model FT/IR-4700AC Fourier-transform infrared spectrometer. Analytical chiral HPLC was carried out on a JASCO EXTREMA HPLC method scouting system equipped with a JASCO PU-4180 quaternary pump, a JASCO UV-4075 UV-vis detector, a JASCO CD-4095 CD detector, a JASCO AS-4050 autosampler, a JASCO CO-4065 column oven using DAICEL CHIRALPAK® IA-3, IB N-3, IC-3, ID-3, IE-3, IF-3, IG-3, IH, IJ-3 and IK columns (diameter: 4.6 mm; length: 250 mm). Recycling preparative chiral HPLC was carried out on a Japan Analytical Industry LC-7080 Plus recycling preparative HPLC system, equipped with DAICEL CHIRALPAK® IG column (diameter: 20 mm; length: 250 mm). High-resolution matrix assisted laser desorption/ionization time of flight (MALDI-TOF) mass spectrometry measurements were performed on a JEOL model JMS-S3000 mass spectrometer. Analytical SEC was performed at 40 °C on a Shimadzu LC-20AT, CBM-20A, CTO-20A equipped with a column (Shodex KF-804L), a refractive index (RI) detector (a Shimadzu RID-20A) and a UV-vis detector (a Shimadzu SPD-M20A), where chloroform ($CHCl_3$) was used as an eluent at a flow rate of 1.0 mL/min. A molecular weight calibration curve was obtained using standard polystyrenes (TSKstandard polystyrene, TOSOH). UV-vis absorption spectra were recorded at 25 °C on a JASCO model Jasco V-730 UV-vis spectrophotometer. CD spectra were recorded on a JASCO J-820 spectropolarimeter. Differential scanning calorimetry (DSC) measurements were carried out on a Netzsch DSC 204F1, where temperature and enthalpy were calibrated with In (430 K, 3.3 J/mol) and Zn (692.7 K, 12 J/mol) standard samples in sealed Al pans. Thermogravimetric analysis (TGA) was performed on a SHIMADZU model TGA-50 analyzer. Atomic force microscopy (AFM) measurements of the thin-film of the polymers were performed on a Bruker Innova atomic force microscope operated in tapping mode using a silicon cantilever tip (a Bruker OLTESPA-R3). Gwyddion 2.66 software was used for film thickness measurement. 2D GI-XRD on the BL13XU beamline at SPring-8 (Japan Synchrotron Radiation Research Institute, JASRI), using 12.39 keV (λ = 1 Å) X-rays were performed at the grazing incidence angle of 0.12°. 2D diffraction patterns were recorded with a 2D detector, Dectris PILATUS 300K.

3. Theoretical Calculation. Geometry optimization, and UV-vis absorption and CD spectra of the compounds were calculated by DFT and TD-DFT methods, respectively with CAM-

B3LYP/6-311G(d,p) level of theory at S_1 states, using Gaussian 16 program package.[S3] To simplify the calculations, we calculated simplified molecules of **1**s and **6**s where their methoxy tetraethylene glycoloxy moieties were replaced by methoxy moieties (Tables S1–4).

4. CISS Measurement. Spin-polarized magnetic conductive-AFM measurements were performed on a Bruker Innova atomic force microscope equipped with a nonmagnetic sample holder (a Bruker APSH-0020) and a CoCr-cantilever (a Bruker MESP-V2). Disc-shaped Nd magnet was put with up or down magnetization directions on the CoCr-cantilever at a distance of ca. 6 mm, and measured the current-voltage (*I-V*) curve in contact with the surface (Fig. S7). We measured at least fifty *I-V* curves in different location of samples. HOPG substrates were purchased from Bruker (ZYB grade) and freshly cleaved just before use. The cantilever was replaced when changing thin films to keep using a fresh cantilever.

5. Synthesis.

4,9-diphenyl-4,9-dihydro-*s*-indaceno[1,2-*b*:5,6-*b*'] dithiophene-4,9-diol (4). Under N_2, a hexane solution of *n*-BuLi (2.6 M, 6.3 mL, 16.3 mmol) was dropwise added at –78 °C to an anhydrous THF solution (80 mL) of bromobenzene (3.2 g, 20.4 mmol). After stirring at –78 °C for 1 h, 4,9-dihydro-*s*-indaceno[1,2-*b*:5,6-*b*']-dithiophene-4,9-dione (**3**, 2 g, 6.8 mmol) was added at –78 °C. After stirring at –78 °C for 1 h, the resulting mixture was allowed to warm up to 25 °C and stirred for 12 h. The reaction mixture was poured into ice water and extracted with CH_2Cl_2. A combined organic extract was washed with brine, dried over anhydrous sodium sulfate, and then evaporated to dryness under reduced pressure to give crude **4** as a yellow solid (2.34 g, 5.2 mmol) in 77% yield as a mixture of *syn*- and *anti*-isomers with a ratio of 1:3 (Fig. S1). Due to the low solubility, the crude **4** was used in the next reaction without further purification and separation of isomers: ^{1}H NMR (400 MHz, 298 K, DMSO-d_6): δ (ppm) 7.45 (d, J = 4.9 Hz, 1H for *syn*), 7.44 (d, J = 4.9 Hz, 1H for *anti*), 7.15–7.30 (m, 24H), 6.90 (d, J = 4.9 Hz, 1H for *syn*), 6.87 (dd, J = 4.84, 1H for *anti*), 6.37 (s, 1H for *syn*), 6.34 (s, 1H for *anti*). FT-IR (KBr): ν (cm^{-1}) 3561, 3102, 1448, 1043, 973, 866, 734, 698, 672. MALDI-TOF-mass: calcd. for $C_{28}H_{18}O_2S_2$ $[M]^+$; m/z = 450.0743; found: 450.0753. ^{1}H NMR, FT-IR, and high-resolution MALDI-TOF mass spectra of an isomer mixture of **4** are shown in Figs. S11, S12 and S13, respectively.

Compounds (*S*,*S*)-6 and (*R*,*R*)-6. Under N_2, sodium hydride (60 wt % in mineral oil, 620 mg, 15.4 mmol) was added at 0 °C to an anhydrous *N,N*-dimethylformamide (DMF) solution (140 mL) of diol **4** (1.73 g, 3.83 mmol). After stirring at 0 °C for 1 h, the resulting mixture was allowed to warm up to 25 °C and stirred for 1.5 h. Then, an anhydrous DMF solution (25 mL) of tosylate **5** (7.0 g, 19.2 mmol) was added at 25 °C, and the resulting mixture was stirred at 45 °C for 12 h. The reaction mixture was poured into ice water and extracted with ethyl acetate. A combined organic extract was washed with brine, dried over anhydrous sodium sulfate, and then evaporated to dryness under reduced pressure. The residue was subjected to column

chromatography on silica (ethyl acetate) to allow isolation of *syn*-**6** (racemic mixture) as a yellow oil (550 mg, 0.66 mmol) in 17% yield. Chiral resolution of *syn*-**6** was carried out with preparative chiral HPLC separation using DAICEL CHIRALPAK IG (2.0 cm φ, 25 cm length) using ethyl acetate: hexane = 1:2 as an eluent, to afford enantiomerically pure (*R*,*R*)-**6** and (*S*,*S*)-**6**. Their absolute structures were estimaed by TD-DFT calculations with B3LYP/6-311G(d,p) level of theory (Fig. 2 in the main text). (*S*,*S*)-**6**: ^{1}H NMR (600 MHz, $CDCl_3$): δ (ppm) 7.40 (dd, J =1.38, 6.66 Hz, 2H), 7.25 (m, 4H), 7.20 (s, 1H), 6.89 (d, J = 4.8 Hz, 1H), 3.65 (m, 12H), 3.53 (m, 2H), 3.37 (m, 5H). ^{13}C{^{1}H} NMR (150 MHz, $CDCl_3$): δ (ppm) 151.9, 151.3, 144.1, 141.7, 135.6, 128.3, 128.2, 127.5, 125.7, 122.8, 115.8, 86.0, 71.9, 70.67, 70.63, 70.62, 70.60, 70.52, 63.6, 59.0. FT-IR (KBr): ν (cm^{-1}) 2873, 1454, 1356, 1181, 1103, 922, 700, 553. MALDI-TOF-mass: calcd. for $C_{46}H_{54}O_{10}S_2$ [M]$^{+}$; *m/z* = 830.3153; found: 830.3148. ^{1}H NMR spectrum, ^{1}H-^{1}H COSY correlations, ^{13}C{^{1}H} NMR spectrum, HSQC and HMBC correlations, FT-IR, and high-resolution MALDI-TOF mass spectra of (*S*,*S*)-**6** are shown in Figs. S14, S15, S16, S17, S18, S19 and S20, respectively. (*R*,*R*)-**6**: ^{1}H NMR (600 MHz, $CDCl_3$): δ (ppm) 7.40 (dd, J =1.38, 6.6 Hz, 2H), 7.25 (m, 4H), 7.20 (s, 1H), 6.89 (d, J = 4.86 Hz, 1H), 3.65 (m, 12H), 3.53 (m, 2H), 3.37 (m, 5H). ^{13}C{^{1}H} NMR (150 MHz, $CDCl_3$): δ (ppm) 151.9, 151.3, 144.1, 141.7, 135.6, 128.3, 128.2, 127.5, 125.7, 122.8, 115.8, 86.0, 71.9, 70.67, 70.63, 70.62, 70.60, 70.52, 63.6, 59.0. FT-IR (KBr): ν (cm^{-1}) 2875, 1454, 1356, 1181, 1104, 925, 700, 552. MALDI-TOF-mass: calcd. for $C_{46}H_{54}O_{10}S_2$ [M]$^{+}$; *m/z* = 830.3153; found: 830.3151. ^{1}H NMR spectrum, ^{1}H-^{1}H COSY correlations, ^{13}C{^{1}H} NMR spectrum, HSQC and HMBC correlations, FT-IR, and high-resolution MALDI-TOF mass spectra of (*R*,*R*)-**6** are shown in Figs. S21, S22, S23, S24, S25, S26 and S27, respectively.

Compounds (*S*,*S*)-1 and (*R*,*R*)-1. Anhydrous DMF solution (5 mL) of *N*-bromo succinimide (NBS) was dropwise added at 0 °C to an HPLC-grade $CHCl_3$ solution (35 mL) of (*S*,*S*)-**6** (190 mg, 0.23 mmol) and the resulting mixture was stirred at 0 °C. After stirring at 0 °C for 1 h, the resulting mixture was allowed to warm up to 25 °C and stirred for 1 h. The reaction mixture was poured into NaOH aqueous solution (5.0 g in 100 mL) at 0°C, and extracted with $CHCl_3$. A combined organic extract was washed with brine, dried over anhydrous sodium sulfate, and then evaporated to dryness under reduced pressure. The residue was subjected to column chromatography on silica (ethyl acetate) to allow isolation of (*S*,*S*)-**1** as a yellow oil (201 mg, 0.20 mmol) in 87% yield. (*R*,*R*)-**1** was obtained with same procedure as a yellow oil (190 mg, 0.19 mmol) in 90% yield. (*S*,*S*)-**1**: ^{1}H NMR (600 MHz, $CDCl_3$): δ (ppm) 7.40 (dd, J =1.4, 6.2 Hz, 2H), 7.29 (m, 3H), 7.15 (s, 1H), 6.92 (s, 1H), 3.68 (m, 12H), 3.55 (m, 2H), 3.38 (m, 5H). ^{13}C{^{1}H} NMR (150 MHz, $CDCl_3$): δ (ppm) 150.9, 150.6, 144.0, 140.9, 135.5, 128.4, 127.8, 125.7, 125.6, 115.8, 114.7, 86.6, 71.9, 70.71, 70.66, 70.64, 70.53, 70.49, 63.8, 59.0. FT-IR (KBr): ν (cm^{-1}) 2919, 2869, 1486, 1468, 1446, 1351, 1321, 1109, 741, 701. MALDI-TOF-mass: calcd. for $C_{46}H_{52}O_{10}S_2Br_2$ [M]$^{+}$; *m/z* = 986.1363; found: 986.1359. ^{1}H NMR spectrum, ^{1}H-^{1}H COSY correlations, ^{13}C{^{1}H} NMR spectrum, HSQC and HMBC correlations, FT-IR, and high-resolution MALDI-TOF mass spectra of (*S*,*S*)-**1** are shown in Figs. S28, S29, S30,

S31, S32, S33 and S34, respectively. (*R*,*R*)-**1**: ^{1}H NMR (600 MHz, $CDCl_3$): δ (ppm) 7.40 (dd, J =1.4, 6.2 Hz, 2H), 7.29 (m, 3H), 7.15 (s, 1H), 6.92 (s, 1H), 3.68 (m, 12H), 3.55 (m, 2H), 3.38 (m, 5H). $^{13}C\{^1H\}$ NMR (150 MHz, $CDCl_3$): δ (ppm) 150.9, 150.6, 144.0, 140.9, 135.5, 128.4, 127.8, 125.7, 125.6, 115.8, 114.7, 86.6, 71.9, 70.71, 70.66, 70.64, 70.53, 70.49, 63.8, 59.0. FT-IR (KBr): ν (cm^{-1}) 2919, 2874, 1486, 1468, 1448, 1352, 1326, 1109, 742, 701. MALDI-TOF-mass: calcd. for $C_{46}H_{52}O_{10}S_2Br_2$ $[M]^+$; *m/z* = 986.1363; found: 986.1361. ^{1}H NMR spectrum, ^{1}H-^{1}H COSY correlations, $^{13}C\{^1H\}$ NMR spectrum, HSQC and HMBC correlations, FT-IR, and high-resolution MALDI-TOF mass spectra of (*S*,*S*)-**1** are shown in Figs. S35, S36, S37, S38, S39, S40 and S41, respectively.

Poly-(*S*,*S*)-1, poly-(*R*,*R*)-1 and poly-*rac*-1. Under nitrogen, (*S*,*S*)-**1** (60.0 mg, 60 μmol), 4,7-bis(4,4,5,5-tetramethyl-1,3,2-dioxaborolan-2-yl)-2,1,3-benzothiadiazole (**2**, 23.6 mg, 60 μmol), K_3PO_4 (258 mg, 1.2 mmol), P(*t*-Bu)$_3$ Pd G2 (6.22 mg, 12 μmol was dissolved in degassed anhydrous THF (1.6 mL) and H_2O (0.4 mL). After stirring at 40 °C for 48 h, the reaction mixture was allowed to be cooled to 25 °C, the reaction mixture was poured into water. A deep bule precipitate formed was collected by filtration. The residue was washed with hot acetone and hexane and extracted with hot $CHCl_3$ by using a Soxhlet extractor to allow isolation of poly-(*S*,*S*)-**1** as a deep blue solid (25 mg, 26.0 μmol) in 30% yield. Poly-(*R*,*R*)-**1** was obtained with same procedure as a deep blue solid (23 mg, 23.9 μmol) in 33% yield. Poly-*rac*-**1** was obtained with the same procedure from *racemic* **1** monomer as a deep blue solid (35 mg, 36.4 μmol) in 35% yield: Poly-(*S*,*S*)-**1**: ^{1}H NMR (400 MHz, 298 K, $CDCl_3$): δ (ppm) 7.96 (s, 1H), 7.84 (s, 1H), 7.50 (m, 2H), 7.25-7.31 (m, 4H), 3.6–3.71 (m, 12H), 3.5 (m, 2H), 3.32 (m, 5H). FT-IR (KBr): ν (cm^{-1}) 2901, 2868, 1486, 1471, 1446, 1384, 1263, 1094,1030, 802, 746, 698. M_n (SEC) = 8,200 Da, M_w/M_n (SEC) = 2.4. ^{1}H NMR spectrum, FT-IR spectrum, and SEC chart of poly-(*S*,*S*)-**1** are shown in Figs. S42, S43 and S44, respectively. Poly-(*R*,*R*)-**1**: ^{1}H NMR (400 MHz, 298 K, $CDCl_3$): δ (ppm) 7.96 (s, 1H), 7.84 (s, 1H), 7.50 (m, 2H), 7.25–7.31 (m, 4H), 3.6–3.71 (m, 12H), 3.5 (m, 2H), 3.32 (m, 5H). FT-IR (KBr): ν (cm^{-1}) 2914, 2867, 1484, 1470, 1451, 1385, 1256, 1095,1032, 804, 749, 701. M_n (SEC) = 10,900 Da, M_w/M_n (SEC) = 2.4. ^{1}H NMR spectrum, FT-IR spectrum, and SEC chart of poly-(*R*,*R*)-**1** are shown in Figs. S45, S46 and S47, respectively. Poly-*rac*-**1**: ^{1}H NMR (400 MHz, 298 K, $CDCl_3$): δ (ppm) 7.96 (s, 1H), 7.84 (s, 1H), 7.50 (m, 2H), 7.25–7.31 (m, 4H), 3.6–3.71 (m, 12H), 3.5 (m, 2H), 3.32 (m, 5H). FT-IR (KBr): ν (cm^{-1}) 2908, 2867, 1485, 1470, 1445, 1381, 1262, 1095,1027, 803, 743, 698. M_n (SEC) = 8,200 Da, M_w/M_n (SEC) = 1.7. ^{1}H NMR spectrum, FT-IR spectrum, and SEC chart of poly-(*R*,*R*)-**1** are shown in Figs. S48, S49 and S50, respectively.

6. Supporting Figures

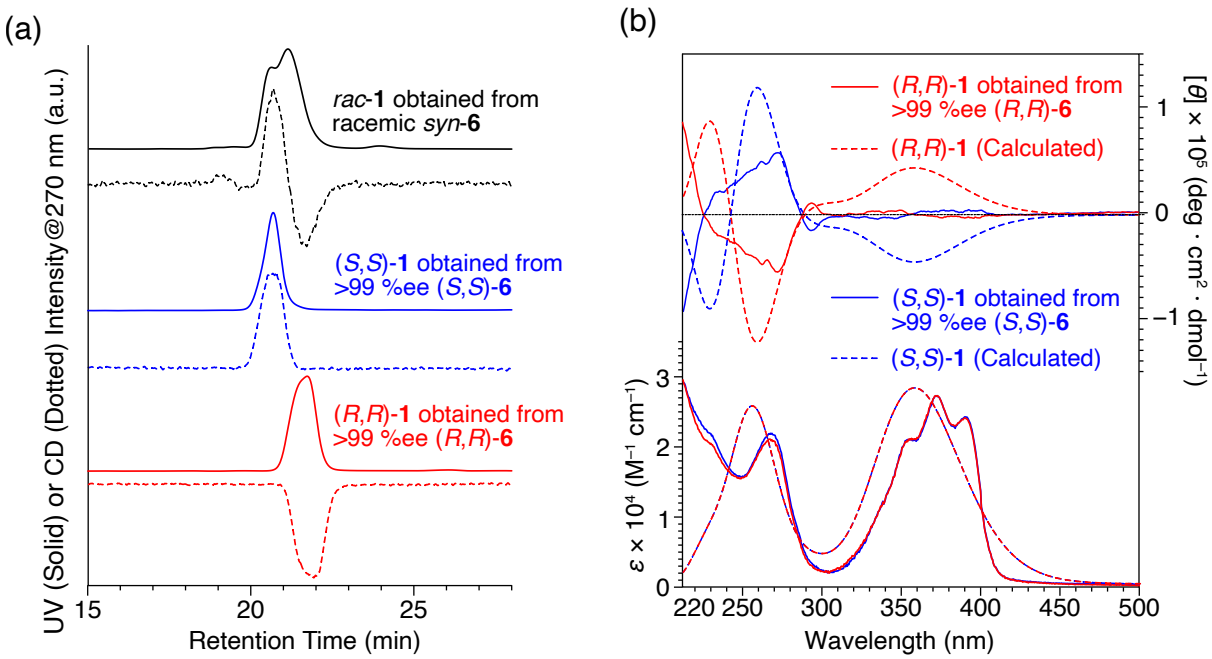

Fig. S1. (a) UV (solid lines, 270 nm) and CD (dotted lines, 270 nm) traces of chiral HPLC analysis (DAICEL Co., Ltd., CHIRALPAK IG-3®, EtOAc:*n*-hexane = 1:2, flow rate = 0.5 mL/min) of *rac*-**1**s (black), (*S*,*S*)-**1** obtained from >99 %ee (*S*,*S*)-**6** (blue) and (*R*,*R*)-**1** obtained from >99 %ee (*R*,*R*)-**6** (red). (b) Experimentally observed (solid lines) and theoretically calculated (dotted lines) CD and UV-vis absorption spectra (15 μM, THF, 25 °C) of (*S*,*S*)-**1** obtained from >99 %ee (*S*,*S*)-**6** (blue) and (*R*,*R*)-**1** obtained from >99 %ee (*R*,*R*)-**6** (red). The chiral HPLC analysis of *rac*-**1** did not result in sufficient base-line separation of enantiomers for preparative chiral resolution, but we can confirm the high optical purity of the optically active **1**s obtained from enantiopure **6**s. Especially, in the profile of (*R*,*R*)-**1**, no CD-positive peak arising from (*S*,*S*)-**1** was observed, indicating that the optical purity of (*R*,*R*)-**1** is >99 %ee. In addition, (*S*,*S*)-**1** obtained from >99 %ee (*S*,*S*)-**6** showed mirror-imaged and same-intensity CD spectra to (*R*,*R*)-**1**, indicating that the optical purity of (*S*,*S*)-**1** is also >99 %ee. Furthermore, the calculated CD spectra was consistent with their chirality. These observations indicate that the bromination reaction from **6**s to **1**s did not cause racemization and stereoinversion.

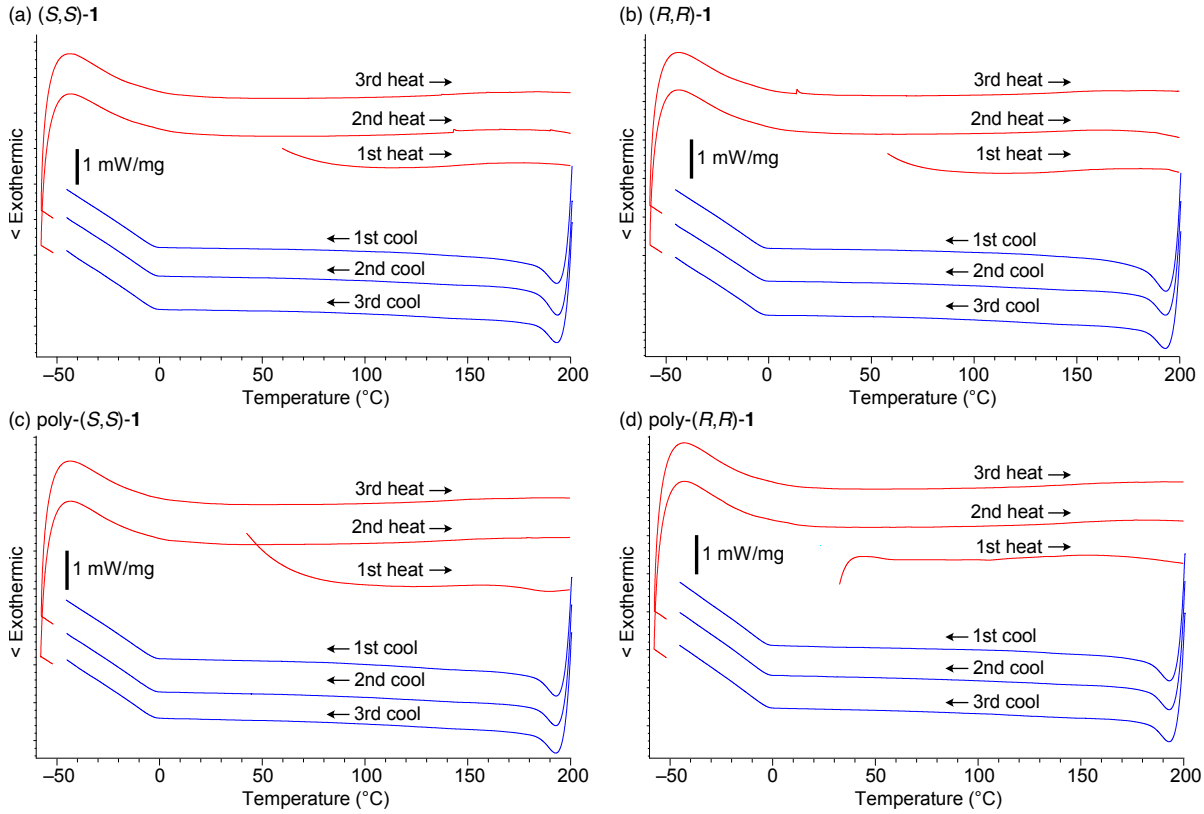

Fig. S2. DSC profiles of (a) (*S*,*S*)-**1**, (b) (*R*,*R*)-**1**, (c) poly-(*S*,*S*)-**1** and (d) poly-(*R*,*R*)-**1** measured at a scan rate of 10 °C/min under N_2 flow (50 mL/min).

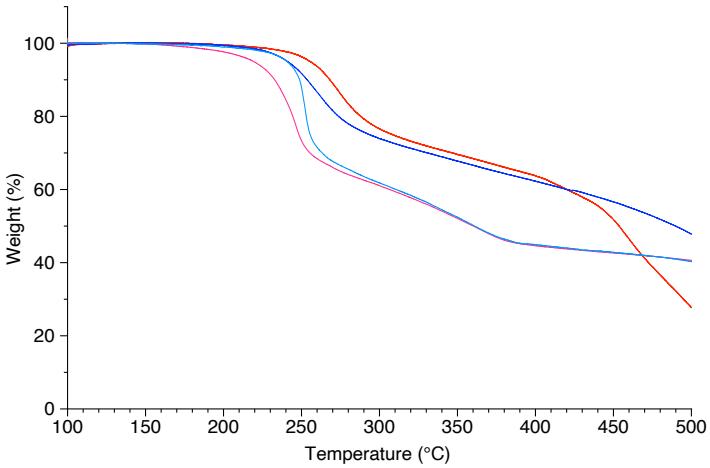

Fig. S3. TGA profiles of (*S*,*S*)-**1** (light blue), (*R*,*R*)-**1** (pink), poly-(*S*,*S*)-**1** (blue) and poly-(*R*,*R*)-**1** (red) measured at a scan rate of 10 °C/min under N_2 flow (50 mL/min).

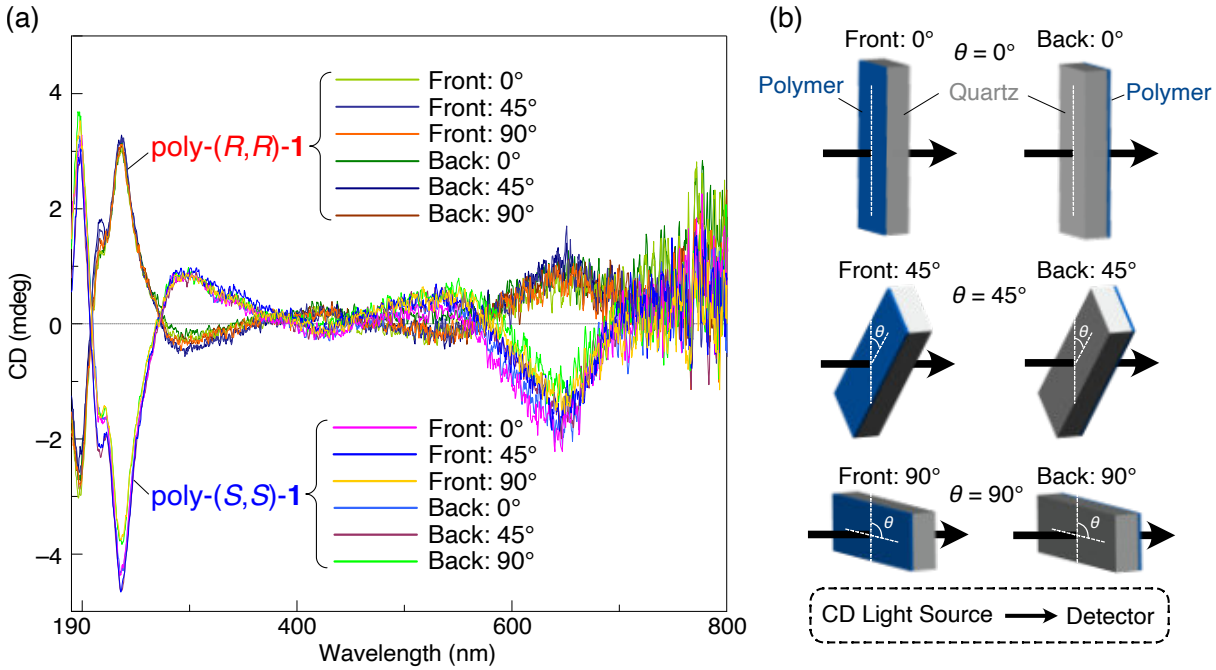

Fig. S4. (a) Incident angle and side dependency of CD spectra of poly-(*S*,*S*)-**1** and poly-(*R*,*R*)-**1** on quartz, and (b) their schematic illustrations.[S4] Almost no angle and side dependency of CD spectra was observed for poly-(*S*,*S*)-**1** and poly-(*R*,*R*)-**1** thin films, indicating their amorphous and isotropic nature.

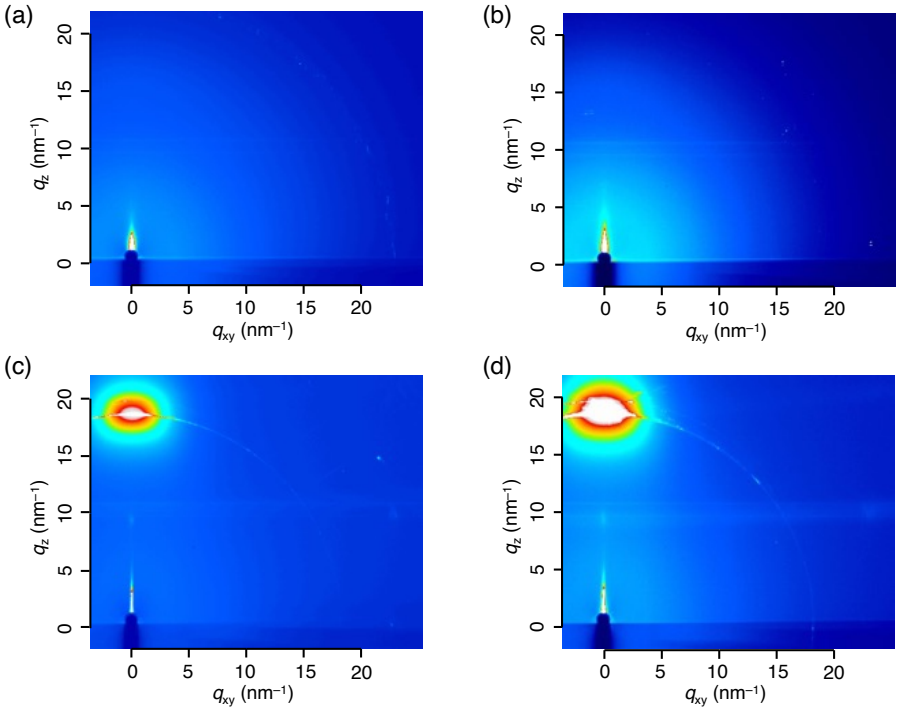

Fig. S5. GI-XRD profiles of (a) poly-(*S*,*S*)-**1** on quartz, (b) poly-(*R*,*R*)-**1** on quartz, (c) poly-(*S*,*S*)-**1** on HOPG and (d) poly-(*R*,*R*)-**1** on HOPG. Strong diffractions at q_z = ca. 17 nm^{-1} in panels c and d are from HOPG substrates. Almost no diffraction was observed for all samples, indicating their amorphous nature.

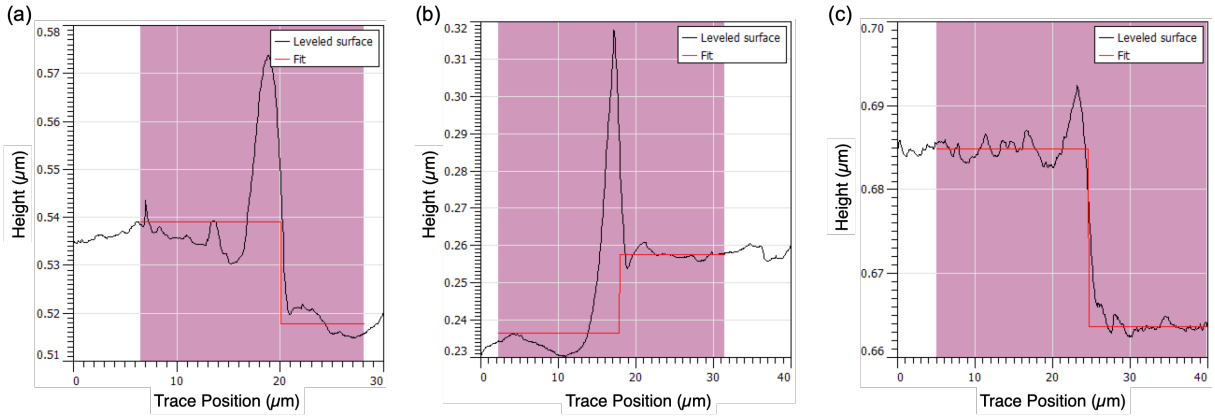

Fig. S6. Representative height profiles obtained in the film thickness measurements of (a) poly-(*S*,*S*)-**1**, (b) poly-(*R*,*R*)-**1** and (c) poly-*rac*-**1** on HOPG. We partially scratched the polymer films and measured the height gaps. The height gaps were measured at least 8 different points and determined to be 23.2 ± 3.2 nm for poly-(*S*,*S*)-**1**, 23.4 ± 4.4 nm for poly-(*R*,*R*)-**1** and 22.1 ± 3.7 nm for poly-*rac*-**1**, respectively.

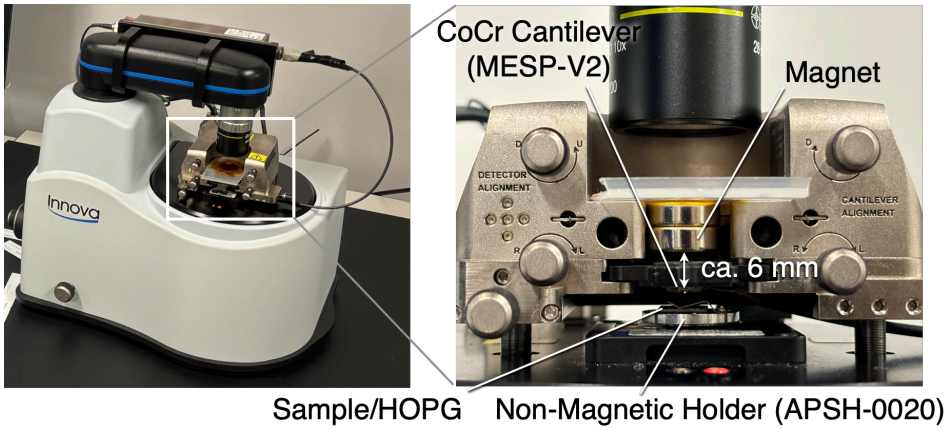

Fig. S7. Experimental setup for spin-polarized mc-AFM measurement.

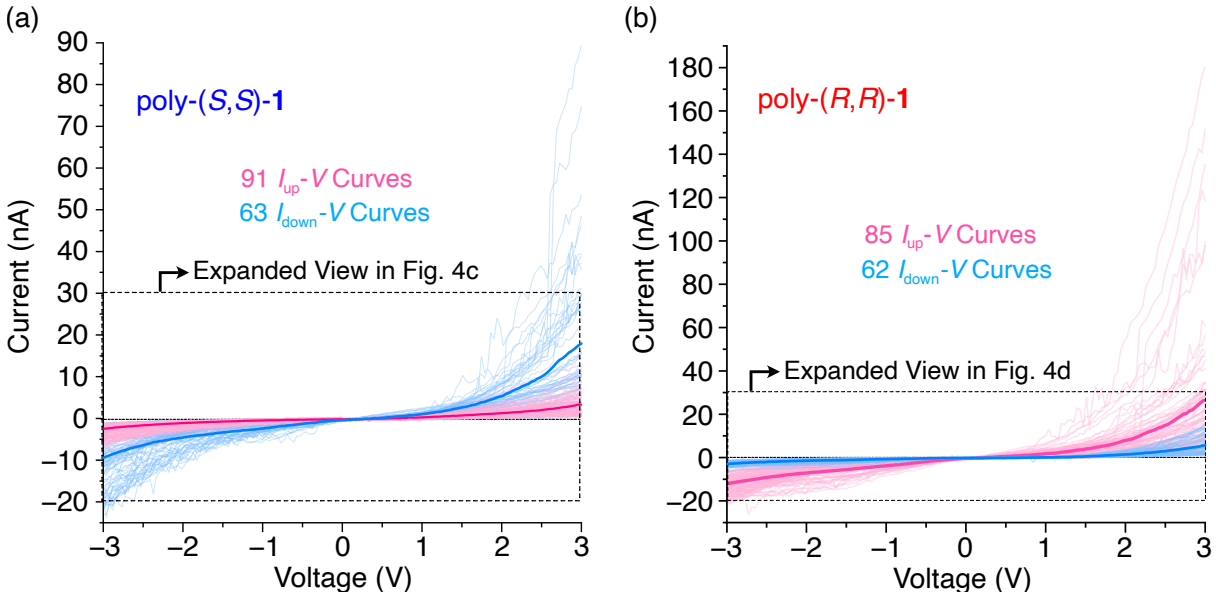

Fig. S8. Full range views of up (pink) or down (sky blue) spin-polarized current-voltage curves of the thin film of (a) poly-(*S*,*S*)-**1** and (b) poly-(*R*,*R*)-**1** on HOPG. Unaveraged curves are shown as thin red and blue lines.

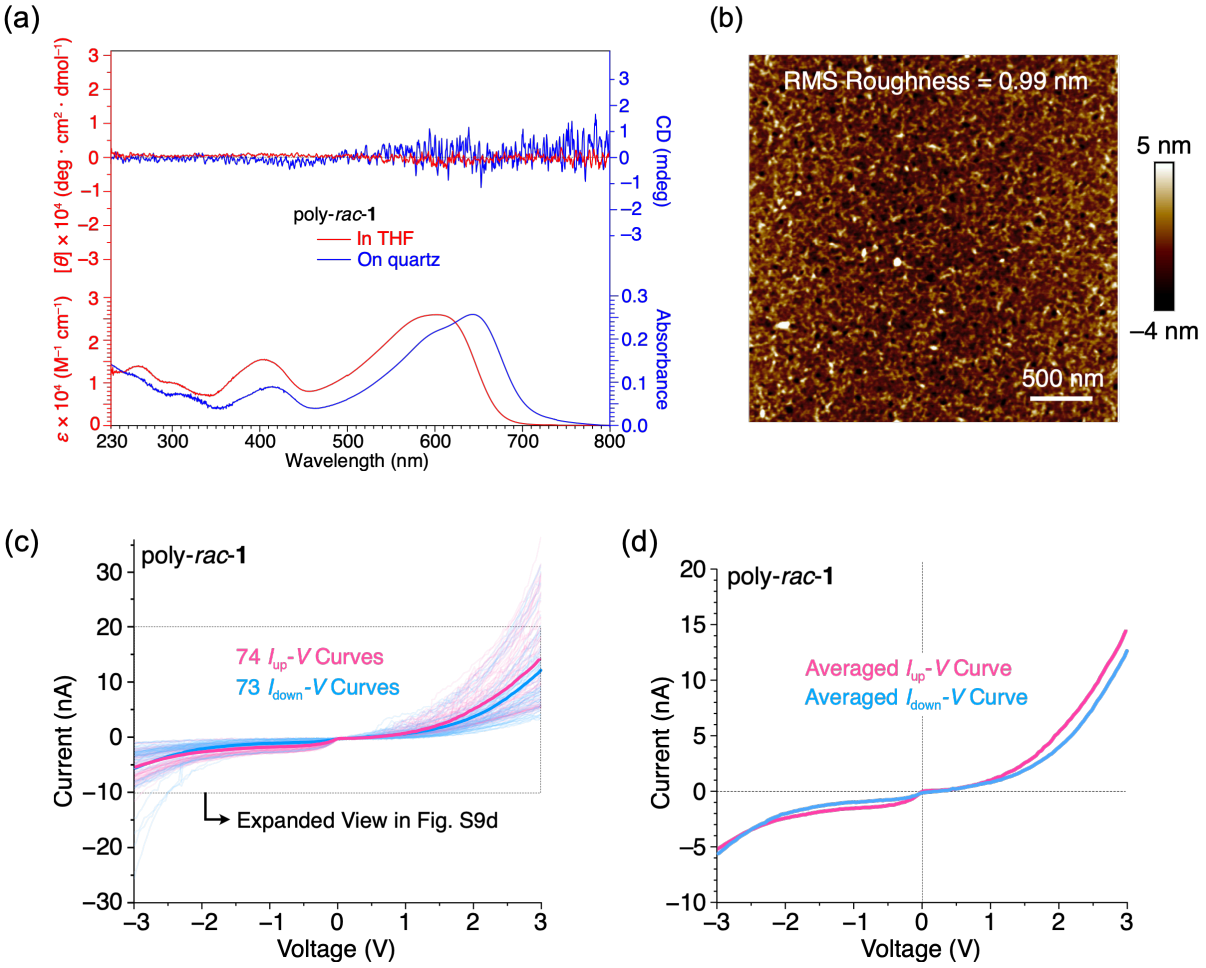

Fig. S9. (a) CD and UV-vis absorption spectra of poly-*rac*-**1** (red) in THF (15 μM for monomer unit, 25 °C) and on quartz (blue). (b) AFM height image of spin-coat thin film of poly-*rac*-**1** on HOPG prepared by spin coating its chlorobenzene solutions (3 mg/mL) at 1500 rpm [film thickness = 22.1 ± 3.7 nm (see Fig. S6c), root mean square roughness = 0.99 nm]. (c) Up (pink) or down (sky blue) spin-polarized current-voltage (I_{up}-V and I_{down}-V) curves of the spin-coat thin film of poly-*rac*-**1** on HOPG. Unaveraged curves are shown as thin red and blue lines. (d) Expanded view of averaged up (pink) or down (sky blue) spin-polarized current-voltage curves of the spin-coat thin film of poly-*rac*-**1** on HOPG. The difference between averaged I_{up}-V and I_{down}-V curves of poly-*rac*-**1** is small, indicating that optically inactive poly-*rac*-**1** exhibits no CISS behavior.

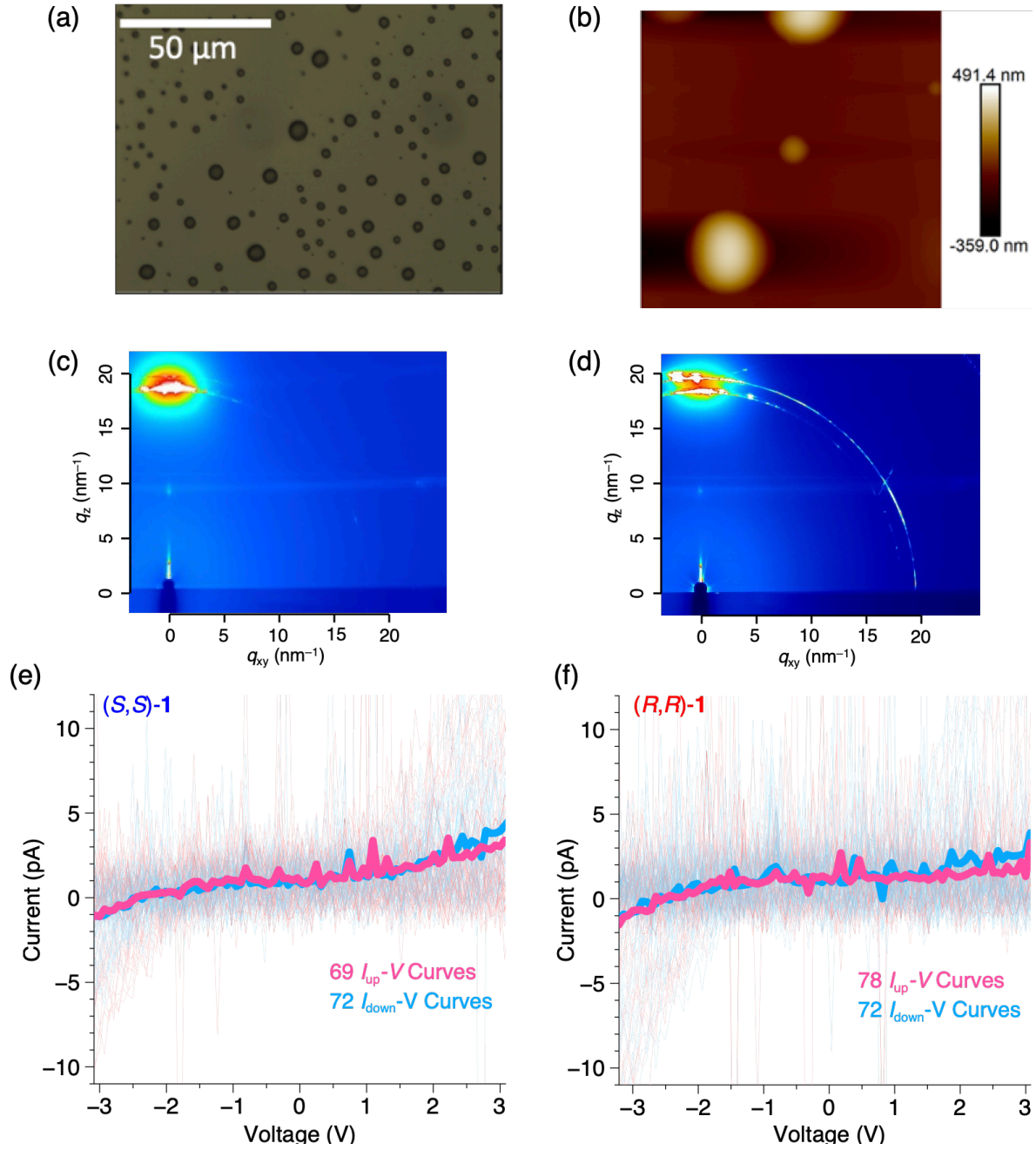

Fig. S10. (a) Optical microscope and (b) AFM images of thin film of (*S*,*S*)-**1** on HOPG. GI-XRD profiles of (c) (*S*,*S*)-**1** and (d) (*R*,*R*)-**1** on HOPG. The thin films of monomers were fabricated by spin coating (chlorobenzene, 3 mg/mL, 1500 rpm). Strong diffractions at q_z = ca. 17 nm^{-1} in panels c and d are from HOPG substrates. Almost no diffraction was observed for all samples, indicating their amorphous nature. Up (pink) or down (sky blue) spin-polarized current-voltage curves of the thin films of (e) (*S*,*S*)-**1** and (f) (*R*,*R*)-**1** on HOPG. Unaveraged curves are shown as thin red and blue lines.

7. Analytical Data

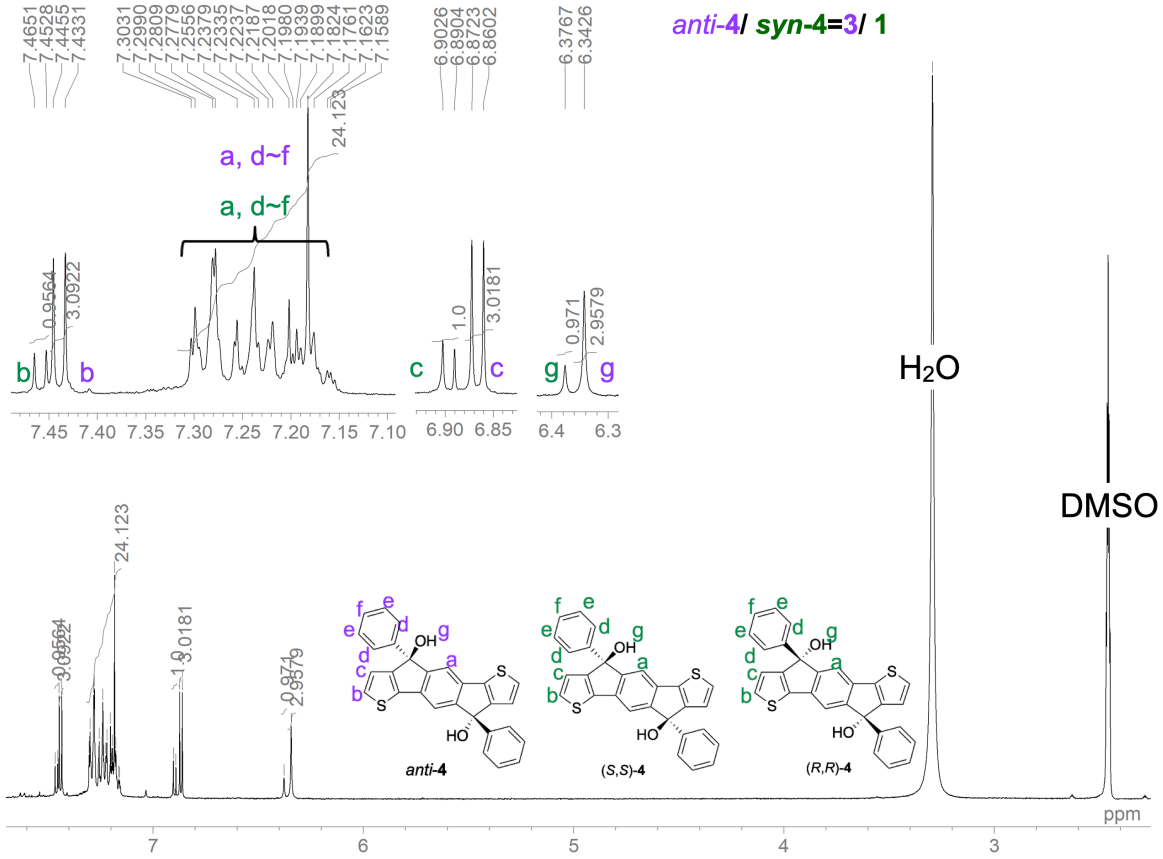

Fig. S11. ^{1}H NMR spectrum (400 MHz) of a mixture of *anti*-**4** and *syn*-**4** (racemic mixture) in DMSO-d_6 at 25 °C.

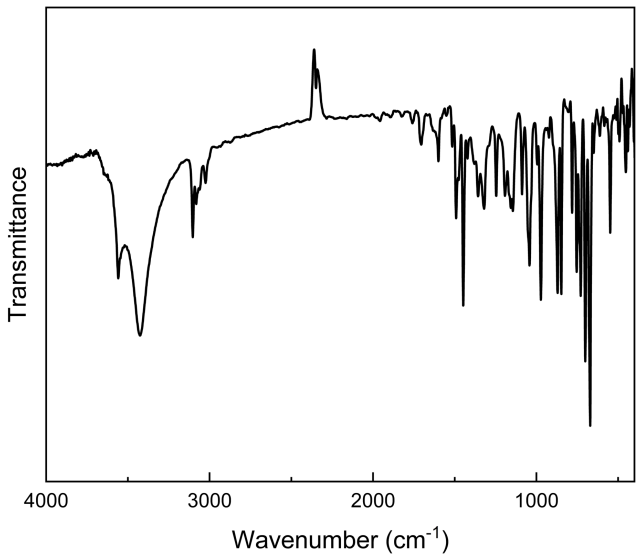

Fig. S12. FT-IR spectrum of a mixture of *anti*-**4** and *syn*-**4** (racemic-mixture) at 25 °C (KBr).

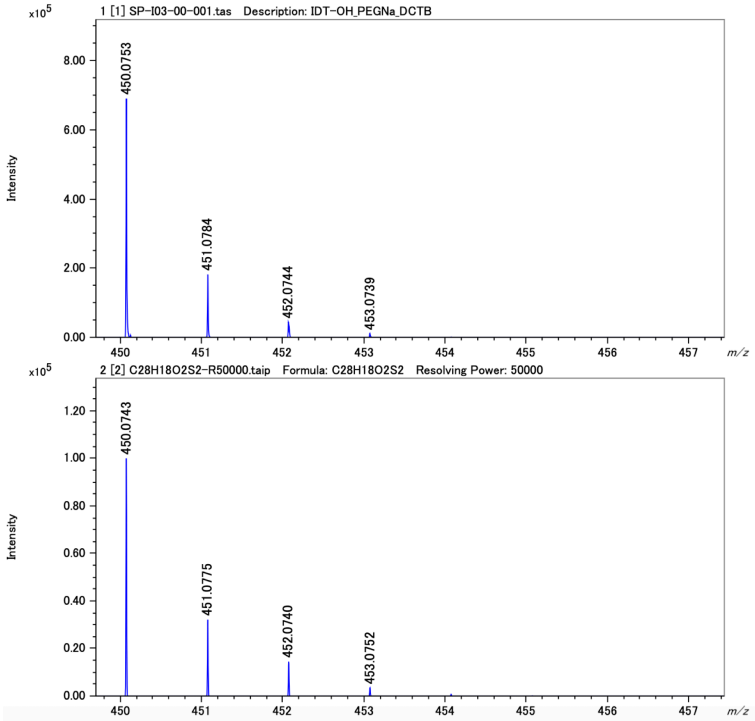

Fig. S13. Observed (upper) and simulated (lower) high-resolution MALDI-TOF mass spectra of a mixture of *anti*-**4** and *syn*-**4** (racemic-mixture).

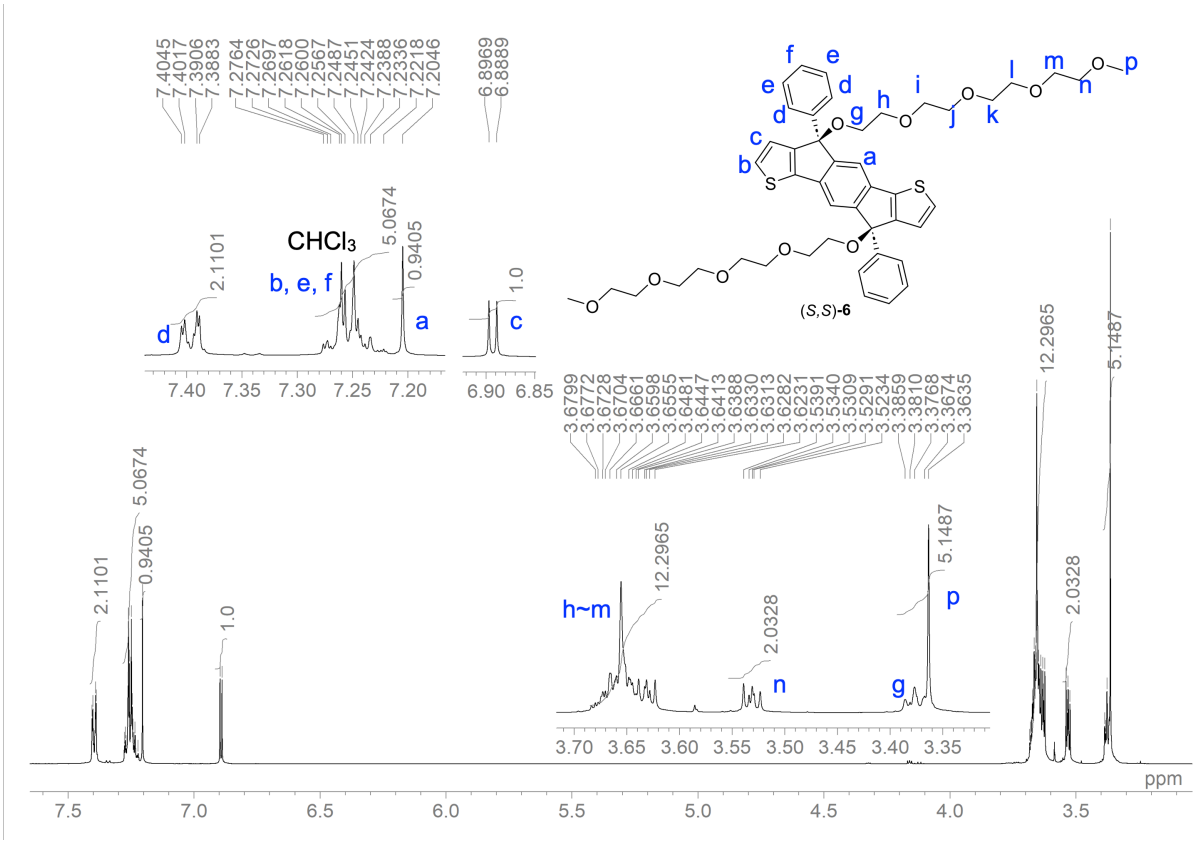

Fig. S14. ^{1}H NMR spectrum (600 MHz) of (*S*,*S*)-**6** in $CDCl_3$ at 25 °C.

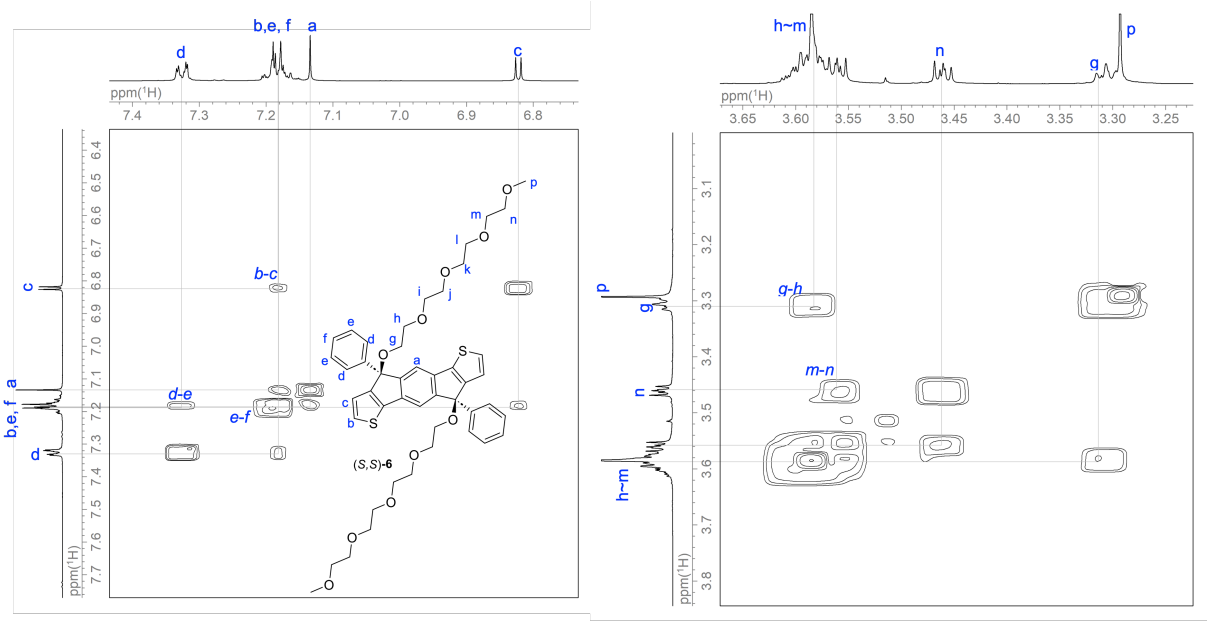

Fig. S15. ^{1}H-^{1}H COSY correlations (600 MHz) of (*S*,*S*)-**6** in $CDCl_3$ at 25 °C.

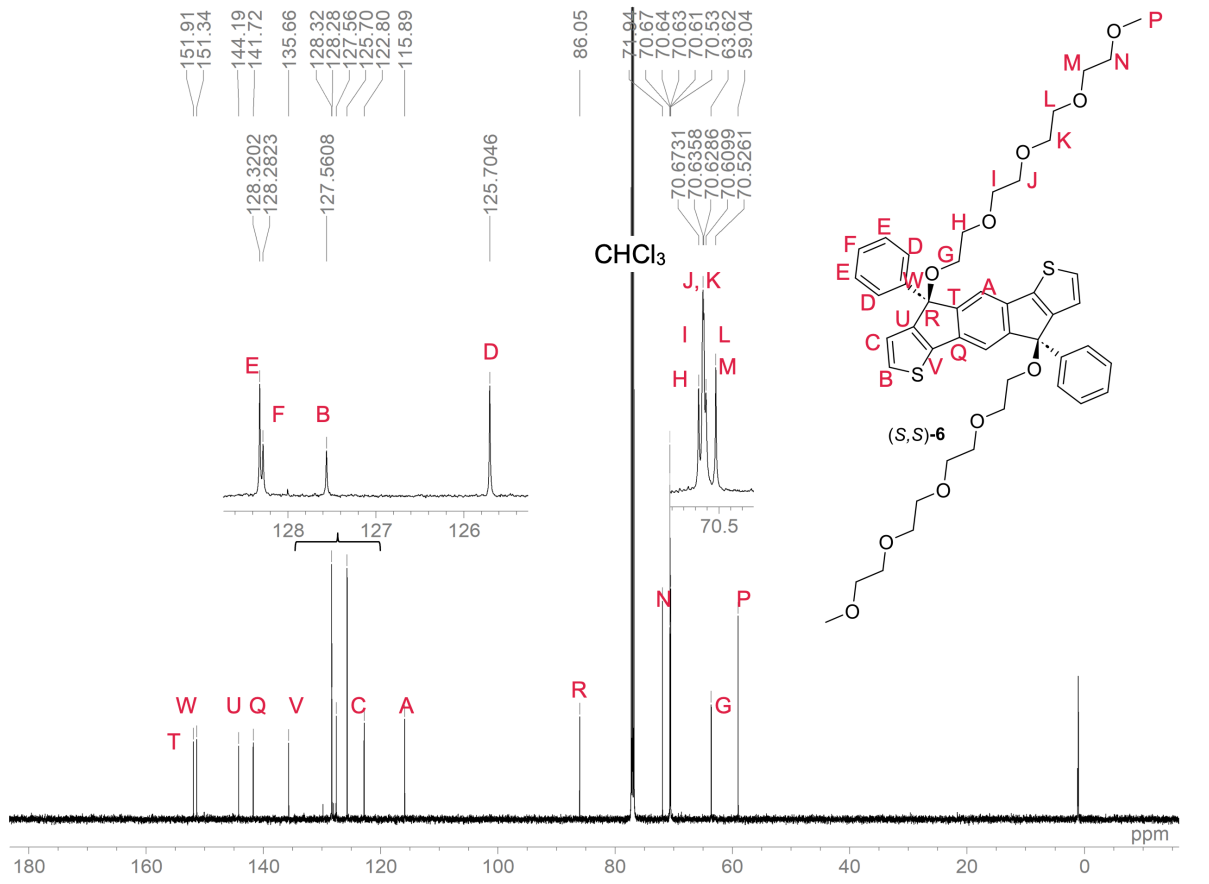

Fig. S16. ^{13}C{^{1}H} NMR spectrum (150 MHz) of (*S*,*S*)-**6** in $CDCl_3$ at 25 °C.

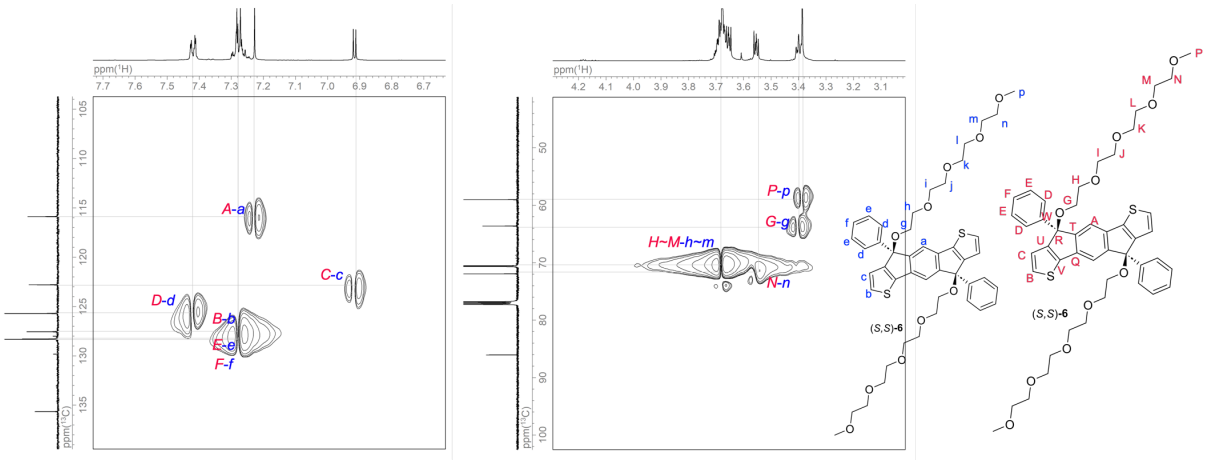

Fig. S17. HSQC correlations (^{1}H; 600 MHz, ^{13}C; 150 MHz) of (*S*,*S*)-**6** in $CDCl_3$ at 25 °C.

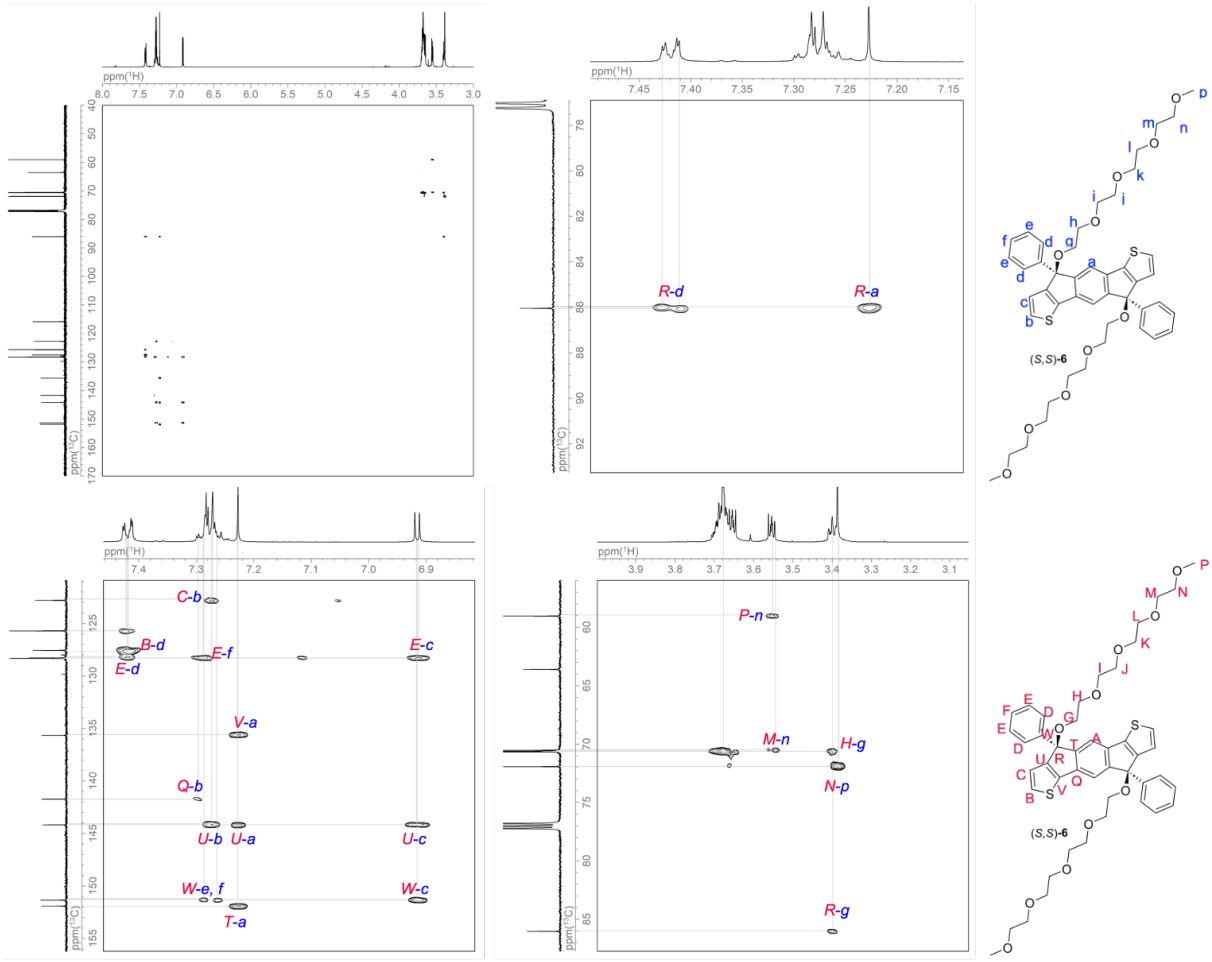

Fig. S18. HMBC correlations (^{1}H; 600 MHz, ^{13}C; 150 MHz) of (*S*,*S*)-**6** in $CDCl_3$ at 25 °C.

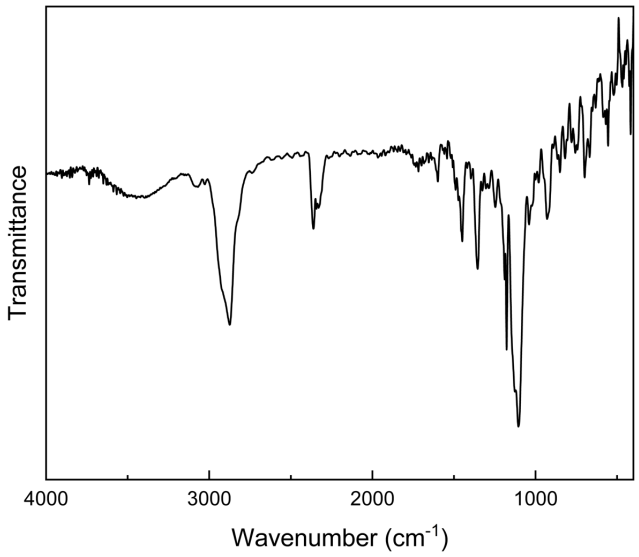

Fig. S19. FT-IR spectrum of (*S*,*S*)-**6** at 25 °C (KBr).

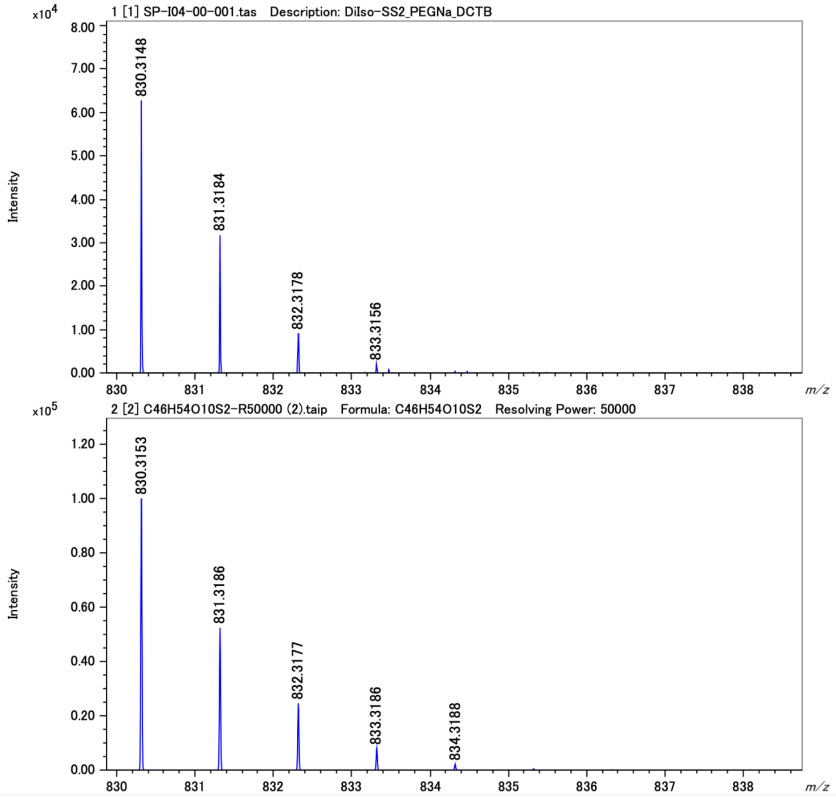

Fig. S20. Observed (upper) and simulated (lower) high-resolution MALDI-TOF mass spectra of (*S*,*S*)-**6**.

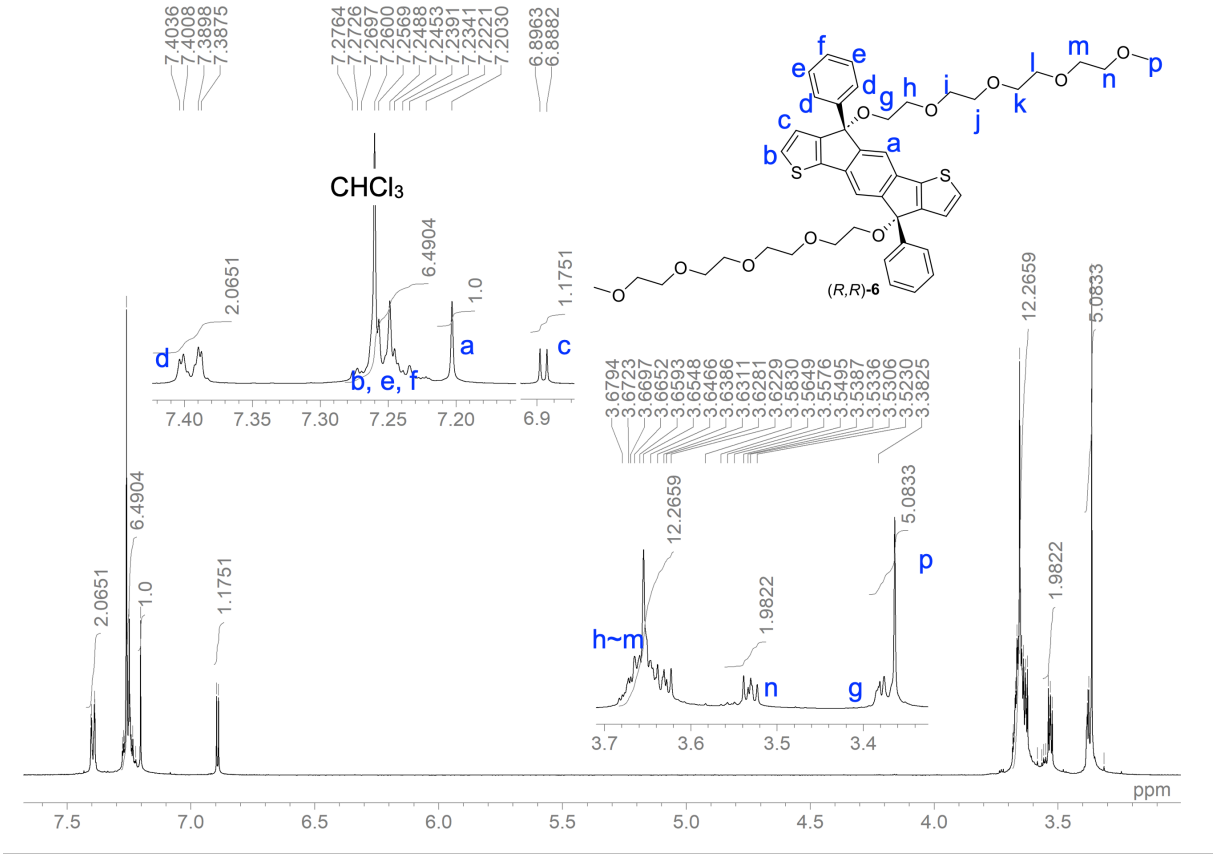

Fig. S21. ^{1}H NMR spectrum (600 MHz) of (*R*,*R*)-**6** in $CDCl_3$ at 25 °C.

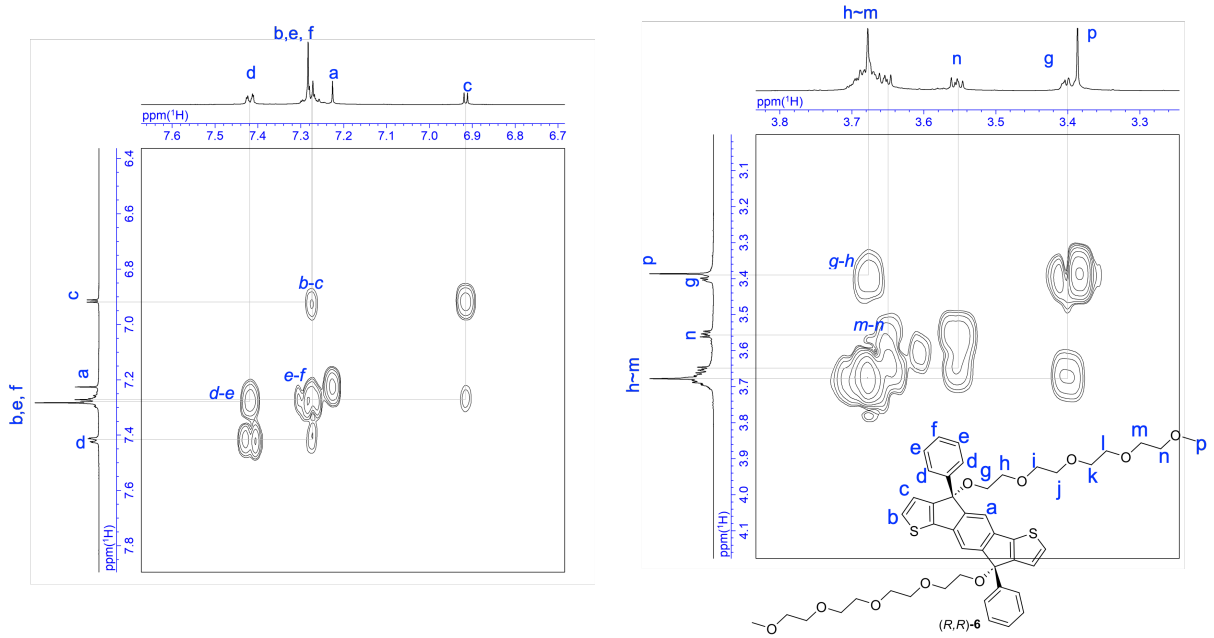

Fig. S22. ^{1}H-^{1}H COSY correlations (600 MHz) of (*R*,*R*)-**6** in $CDCl_3$ at 25 °C.

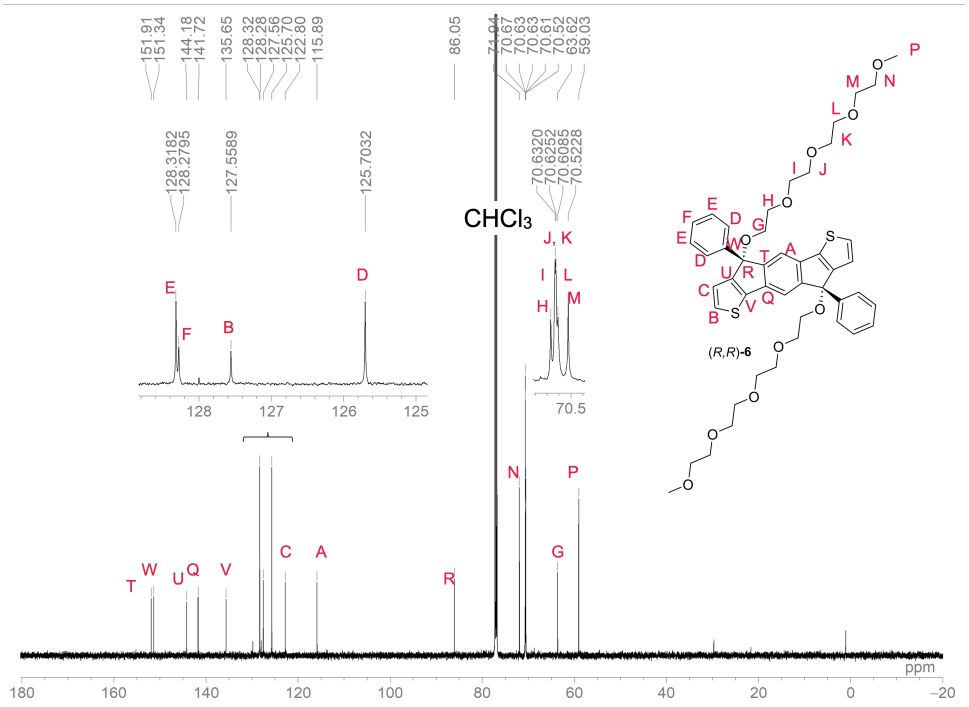

Fig. S23. $^{13}C\{^{1}H\}$ NMR spectrum (150 MHz) of (*R*,*R*)-**6** in $CDCl_3$ at 25 °C.

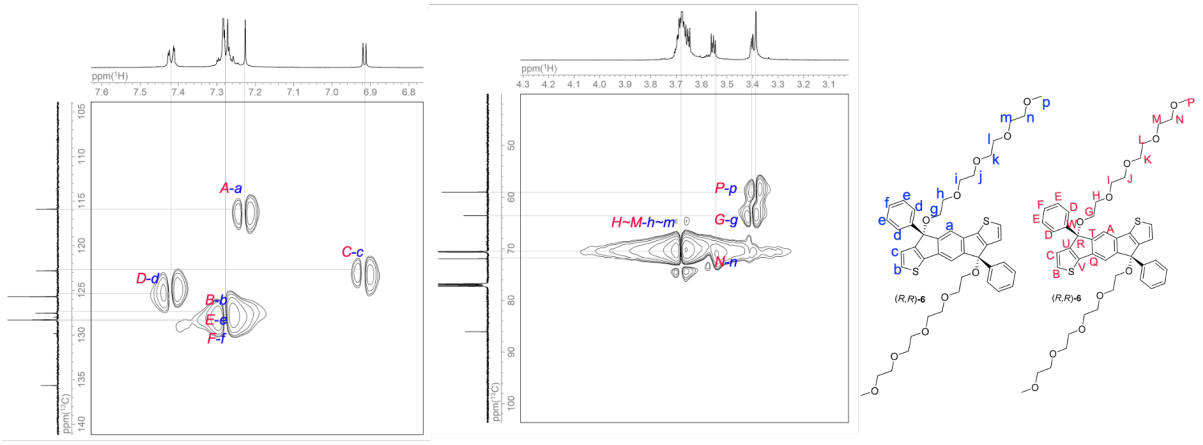

Fig. S24. HSQC correlations (^{1}H; 600 MHz, ^{13}C; 150 MHz) of (*R*,*R*)-**6** in $CDCl_3$ at 25 °C.

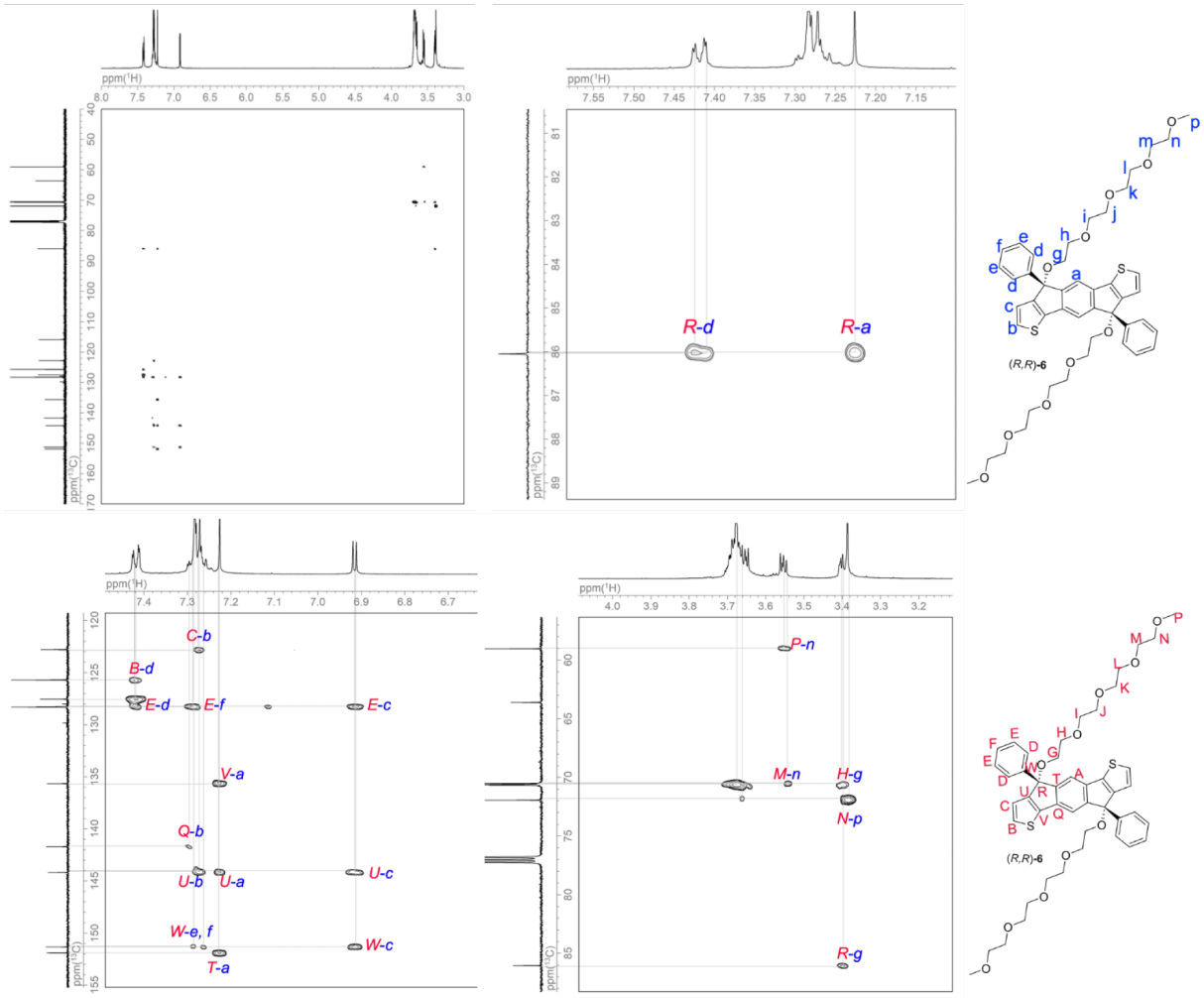

Fig. S25. HMBC correlations (^{1}H; 600 MHz, ^{13}C; 150 MHz) of (*R*,*R*)-**6** in $CDCl_3$ at 25 °C.

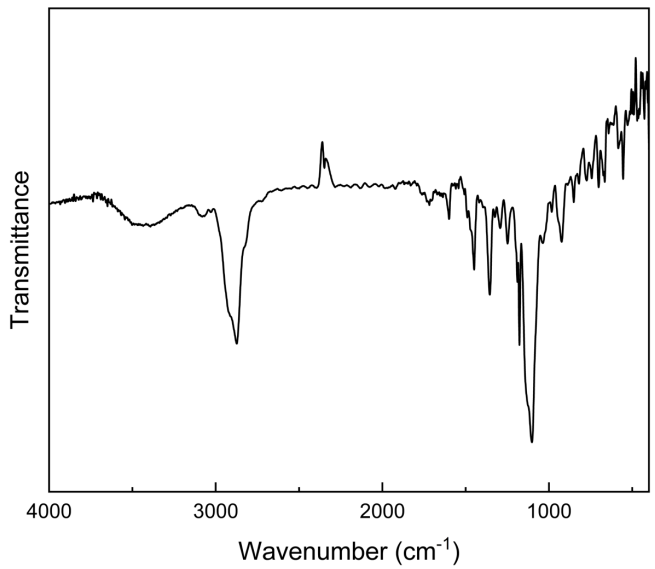

Fig. S26. FT-IR spectrum of (*R*,*R*)-**6** at 25 °C (KBr).

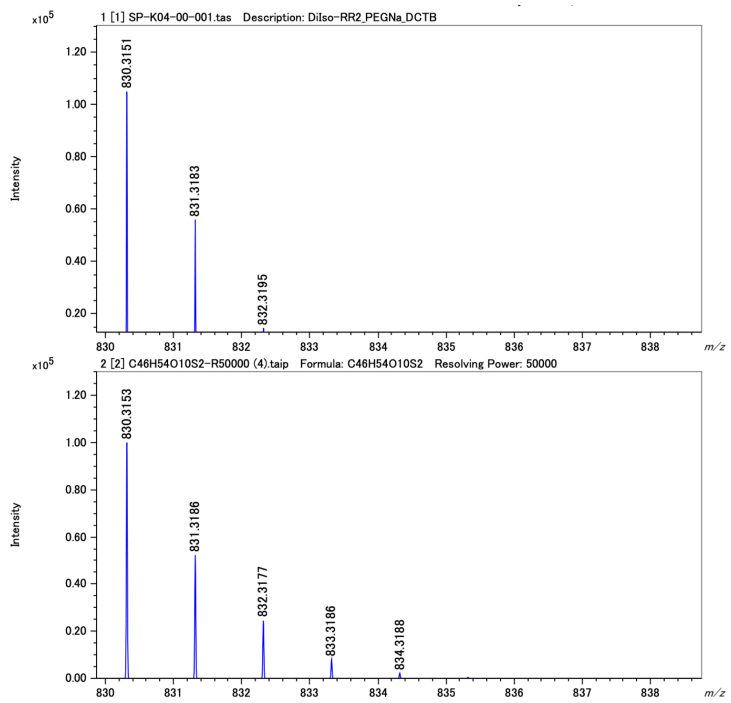

Fig. S27. Observed (upper) and simulated (lower) high-resolution MALDI-TOF mass spectra of (*R*,*R*)-**6**.

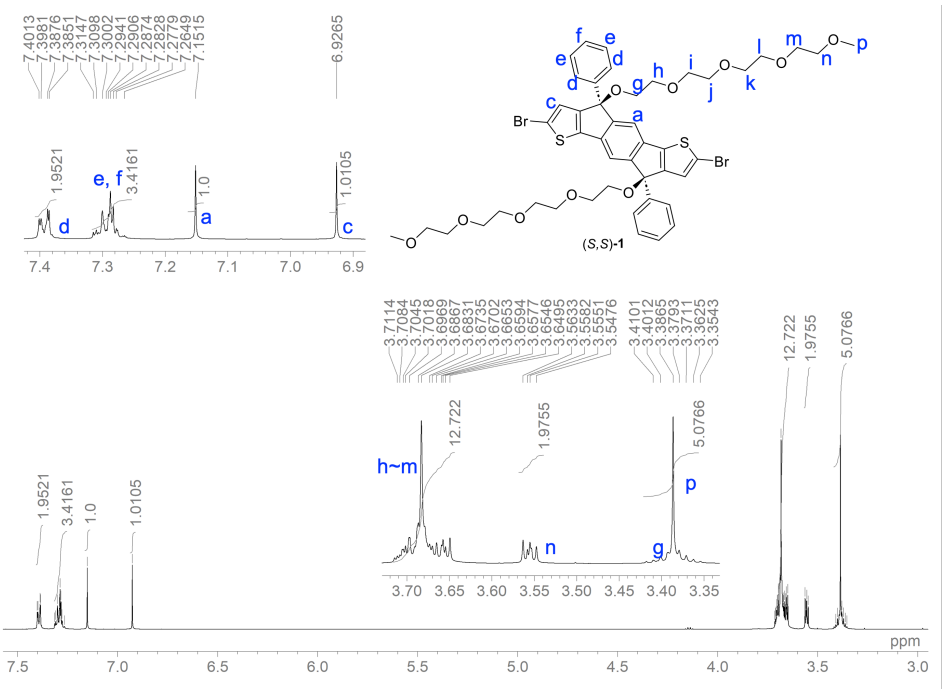

Fig. S28. ^{1}H NMR spectrum (600 MHz) of (*S*,*S*)-**1** in $CDCl_3$ at 25 °C.

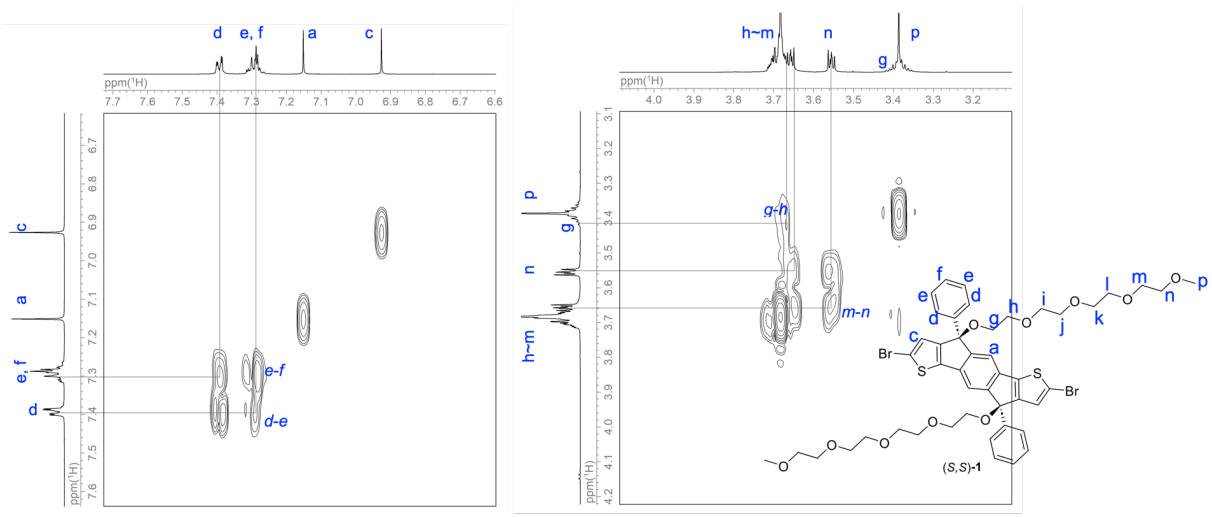

Fig. S29. ^{1}H-^{1}H COSY correlations (600 MHz) of (*S*,*S*)-**1** in $CDCl_3$ at 25 °C.

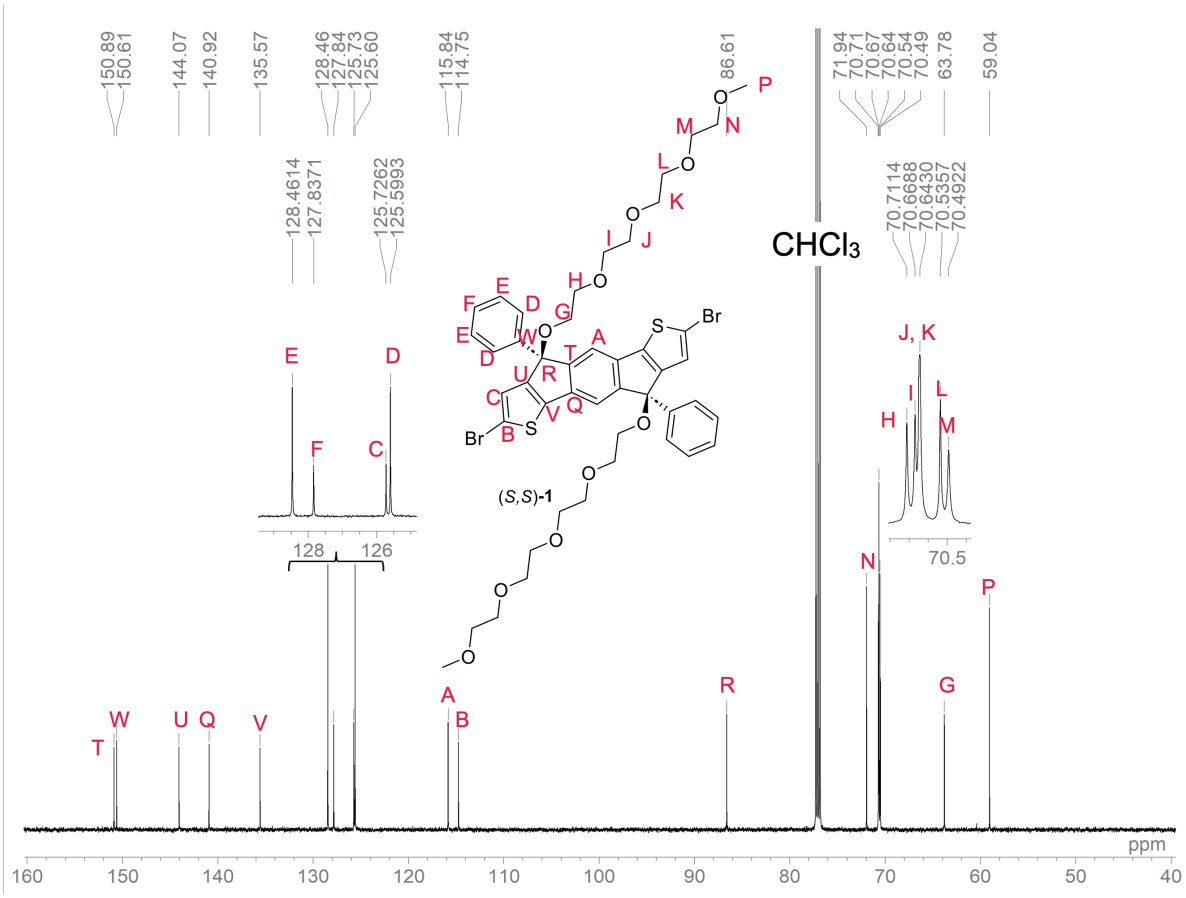

Fig. S30. ^{13}C{^{1}H} NMR spectrum (150 MHz) of (*S*,*S*)-**1** in $CDCl_3$ at 25 °C.

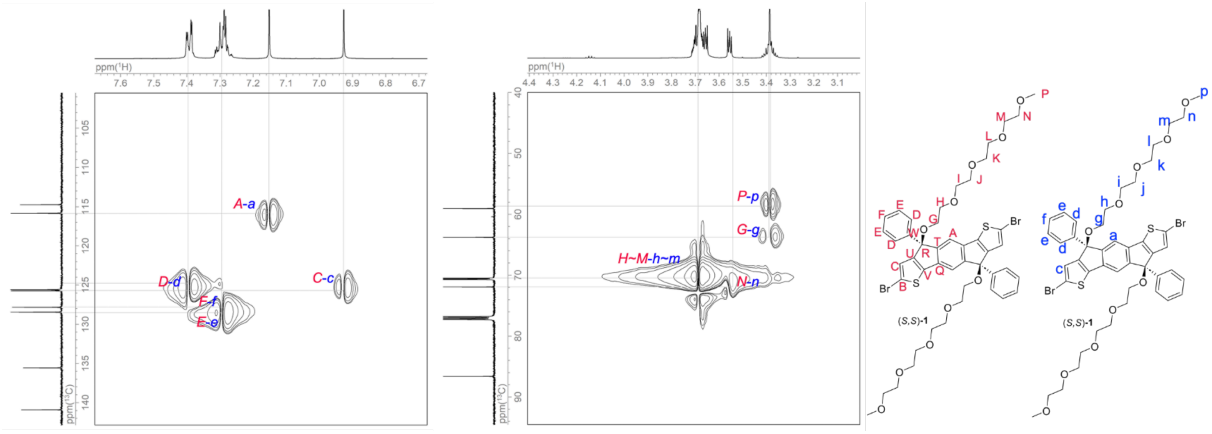

Fig. S31. HSQC correlations (^{1}H; 600 MHz, ^{13}C; 150 MHz) of (*S*,*S*)-**1** in $CDCl_3$ at 25 °C.

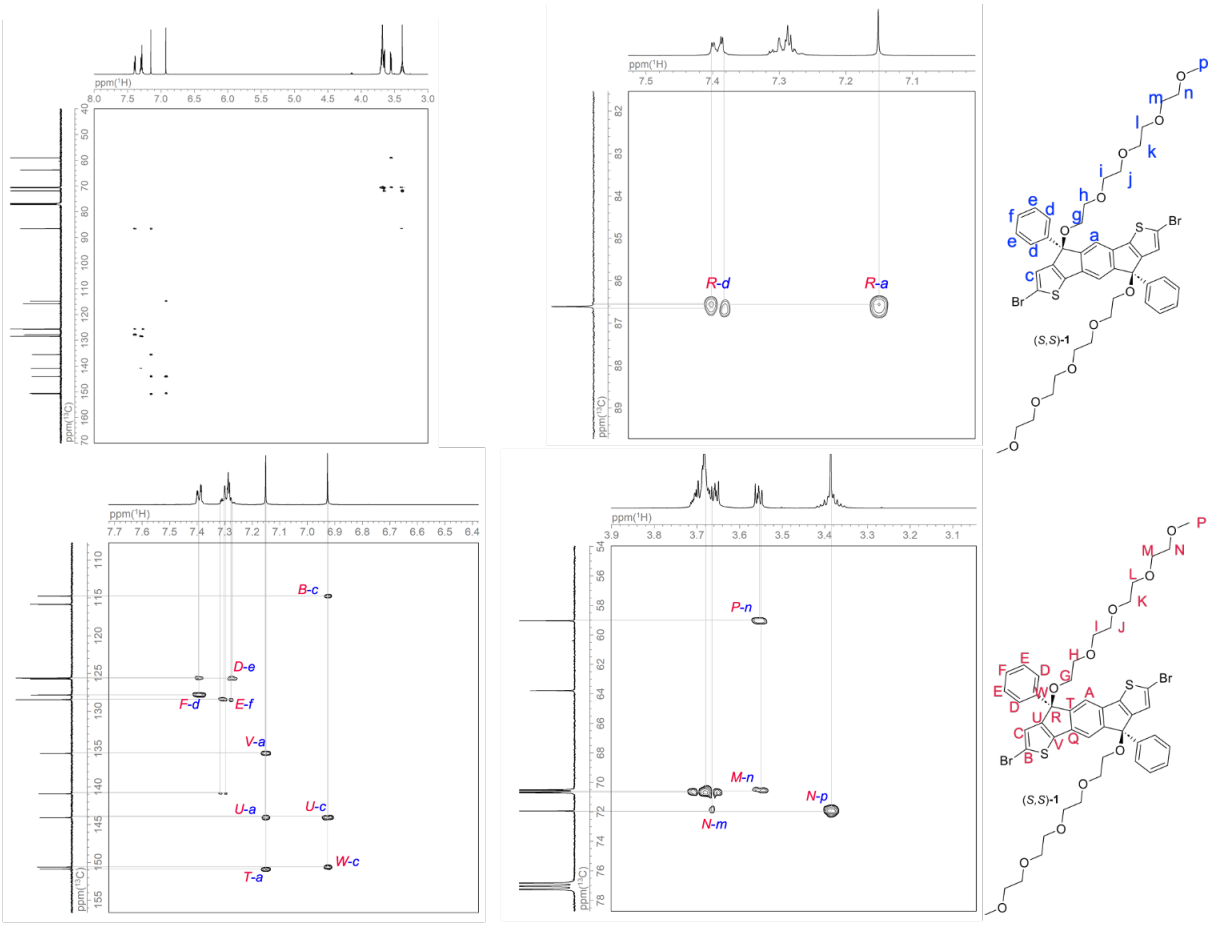

Fig. S32. HMBC correlations (^{1}H; 600 MHz, ^{13}C; 150 MHz) of (*S*,*S*)-**1** in $CDCl_3$ at 25 °C.

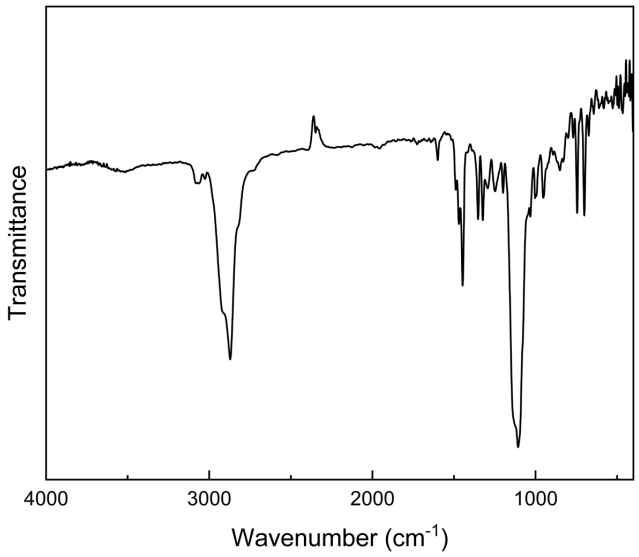

Fig. S33. FT-IR spectrum of (*S*,*S*)-**1** at 25 °C (KBr).

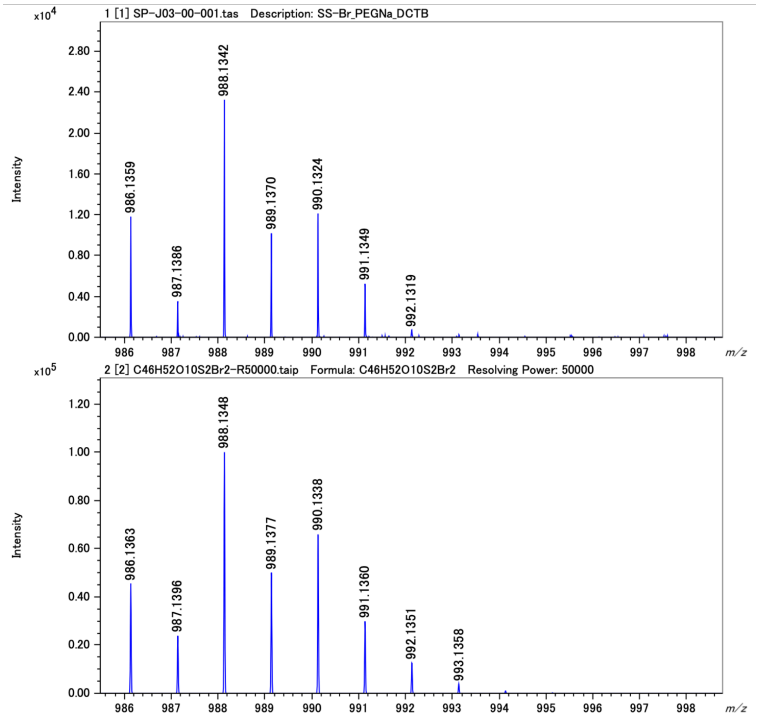

Fig. S34. Observed (upper) and simulated (lower) high-resolution MALDI-TOF mass spectra of (*S*,*S*)-**1**.

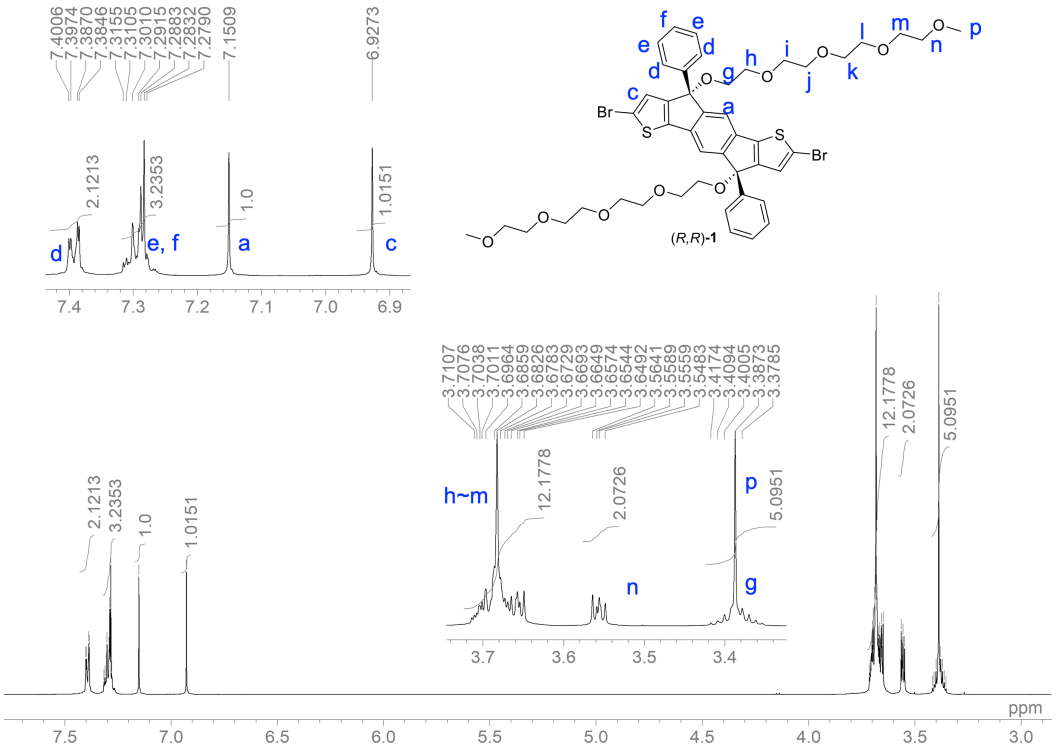

Fig. S35. ^{1}H NMR spectrum (600 MHz) of (*R*,*R*)-**1** in $CDCl_3$ at 25 °C.

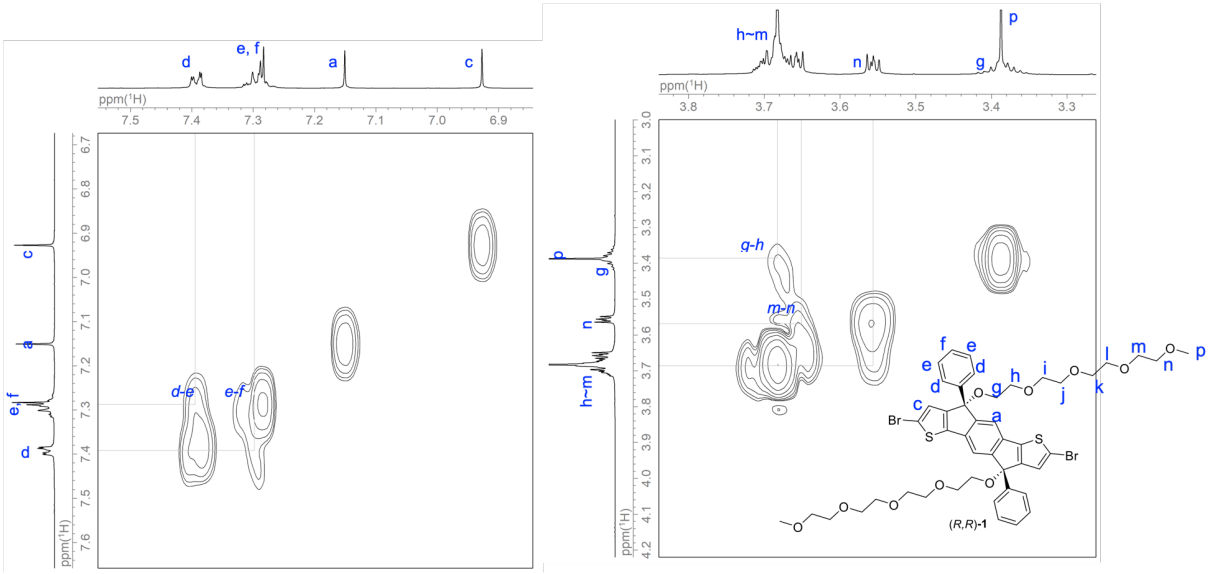

Fig. S36. ^{1}H-^{1}H COSY correlations (600 MHz) of (*R*,*R*)-**1** in $CDCl_3$ at 25 °C.

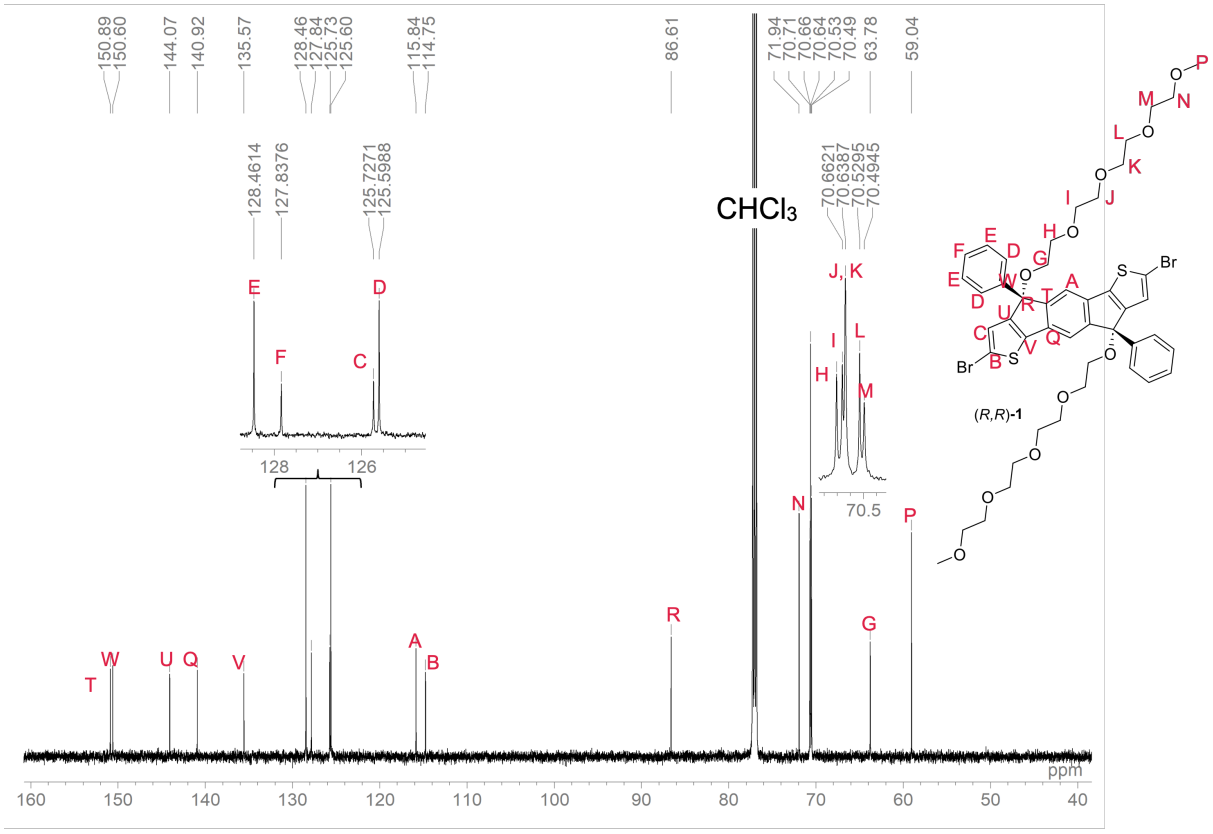

Fig. S37. $^{13}C\{^{1}H\}$ NMR spectrum (150 MHz) of (*R*,*R*)-**1** in $CDCl_3$ at 25 °C.

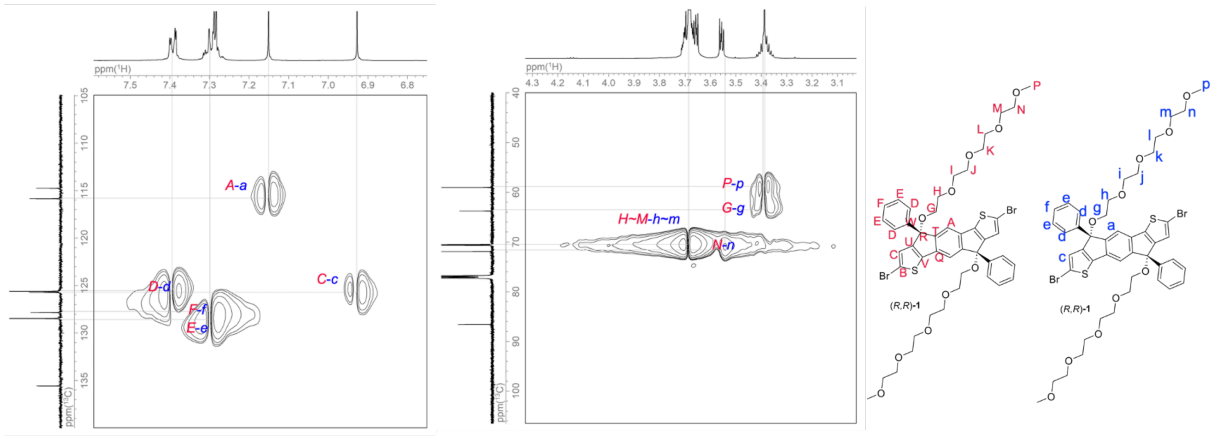

Fig. S38. HSQC correlations (^{1}H; 600 MHz, ^{13}C; 150 MHz) of (*R*,*R*)-**1** in $CDCl_3$ at 25 °C.

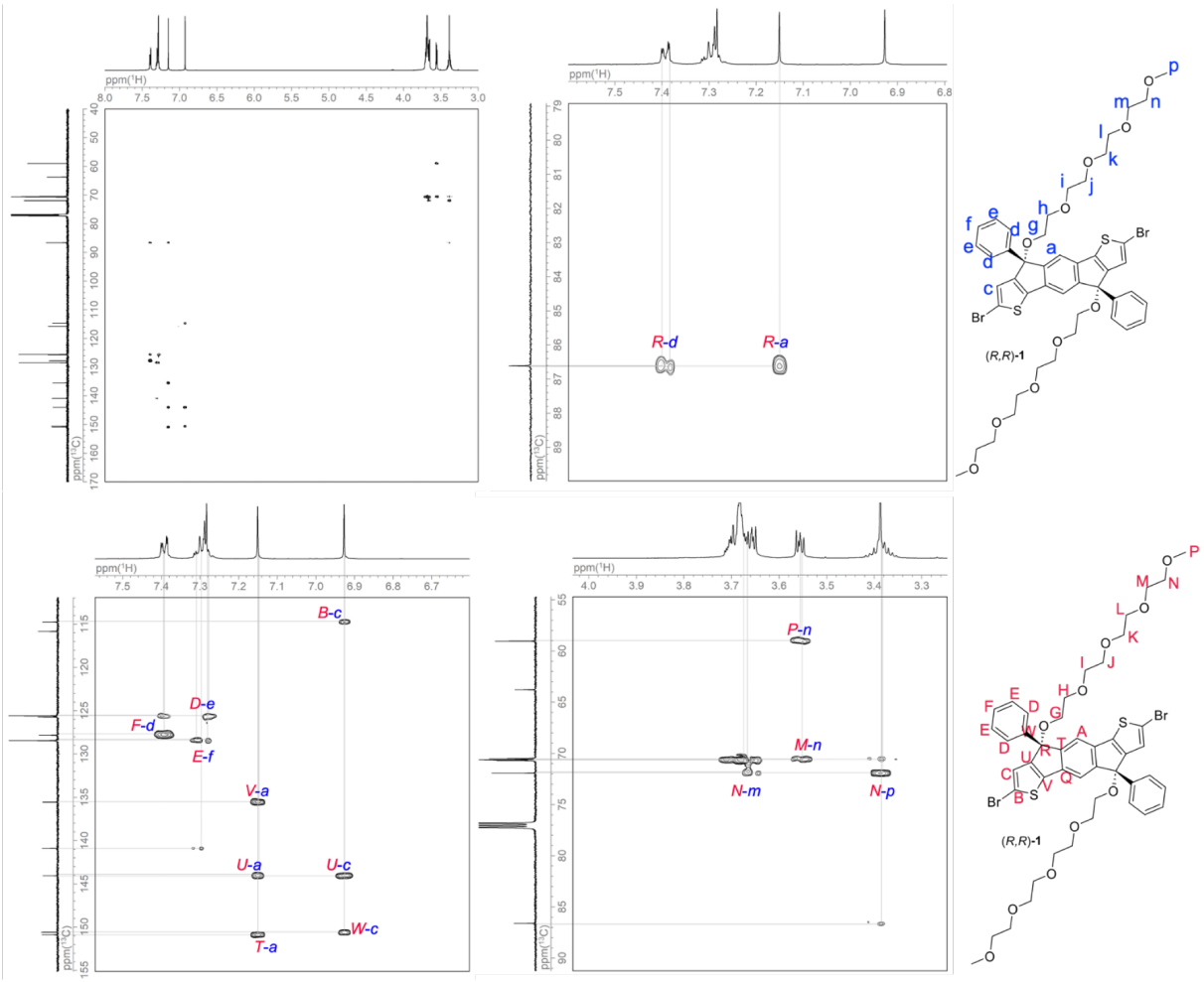

Fig. S39. HMBC correlations (^{1}H; 600 MHz, ^{13}C; 150 MHz) of (*R*,*R*)-**1** in $CDCl_3$ at 25 °C.

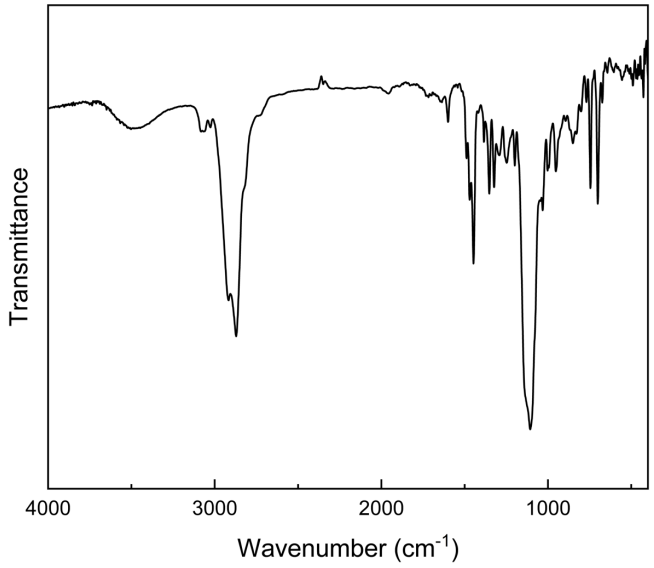

Fig. S40. FT-IR spectrum of (*R*,*R*)-**1** at 25 °C (KBr).

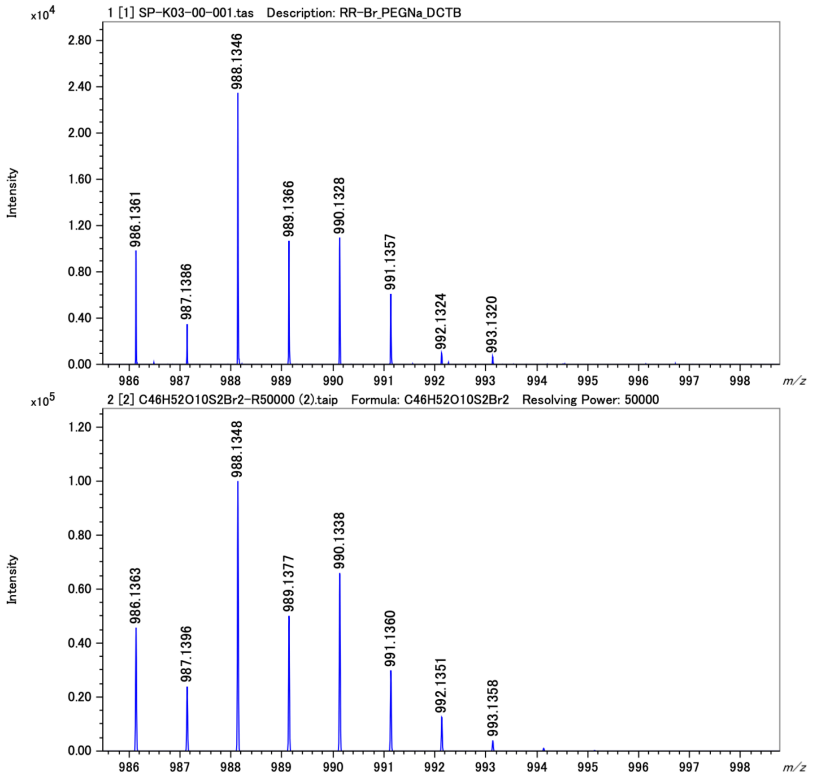

Fig. S41. Observed (upper) and simulated (lower) high-resolution MALDI-TOF mass spectra of (*R*,*R*)-**1**.

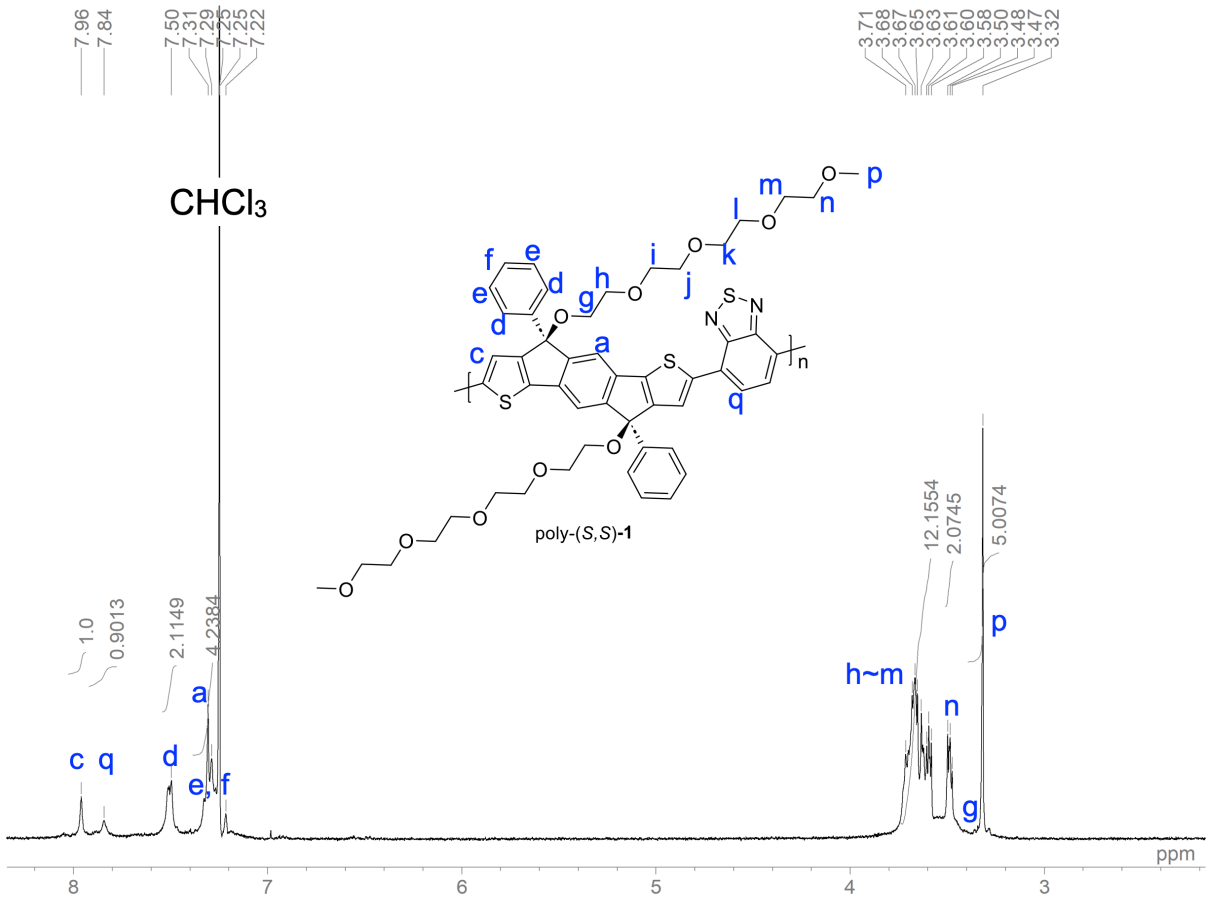

Fig. S42. ^{1}H NMR spectrum (400 MHz) of poly-(*S*,*S*)-**1** in $CDCl_3$ at 25 °C.

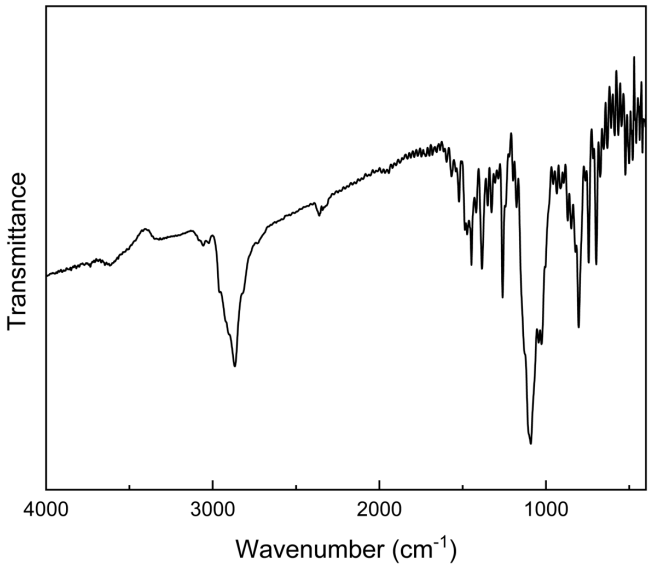

Fig. S43. FT-IR spectrum of poly-(*S*,*S*)-**1** at 25 °C (KBr).

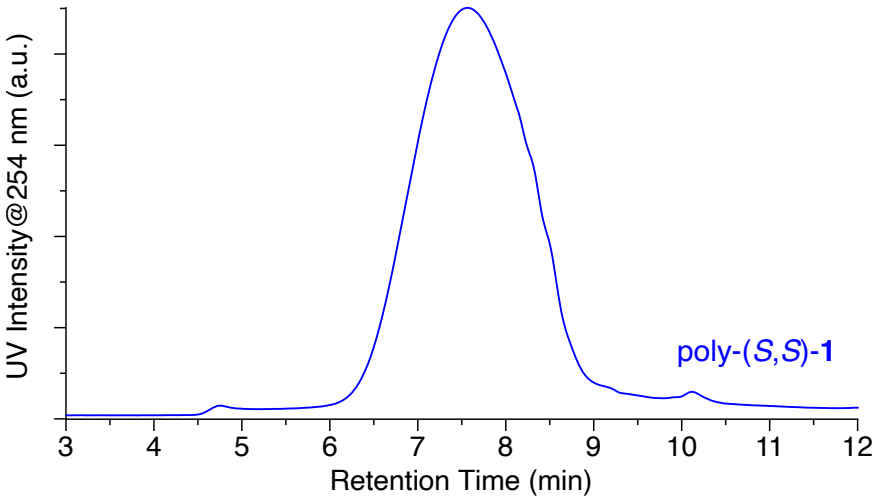

Fig. S44. SEC trace of poly-(*S*,*S*)-**1**.

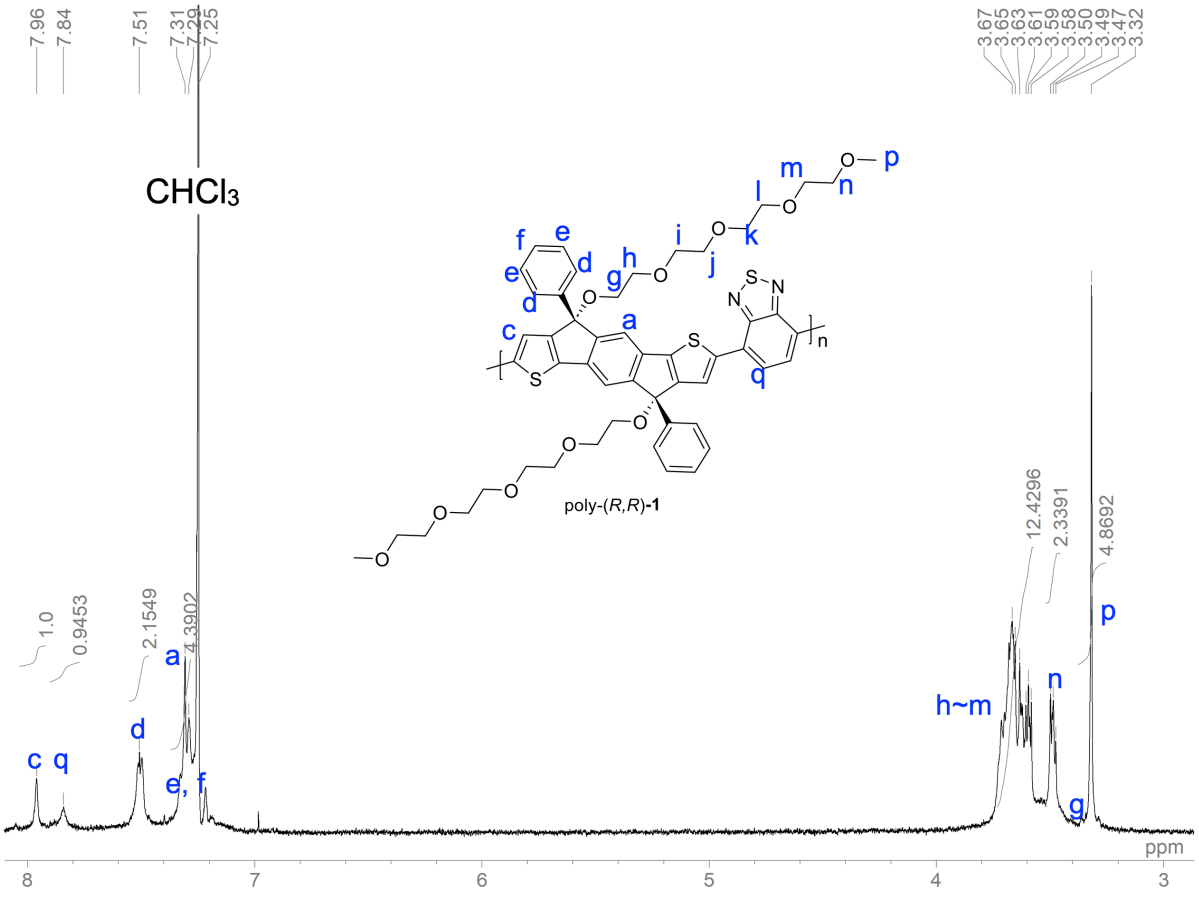

Fig. S45. ^{1}H NMR spectrum (400 MHz) of poly-(*R*,*R*)-**1** in $CDCl_3$ at 25 °C.

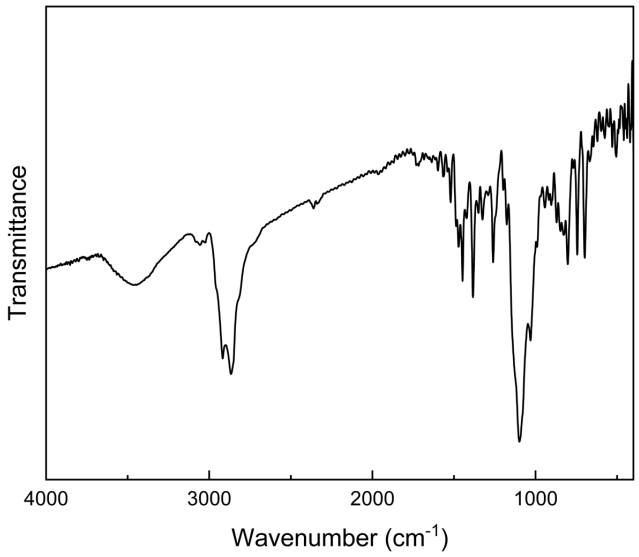

Fig. S46. FT-IR spectrum of poly-(*R*,*R*)-**1** at 25 °C (KBr).

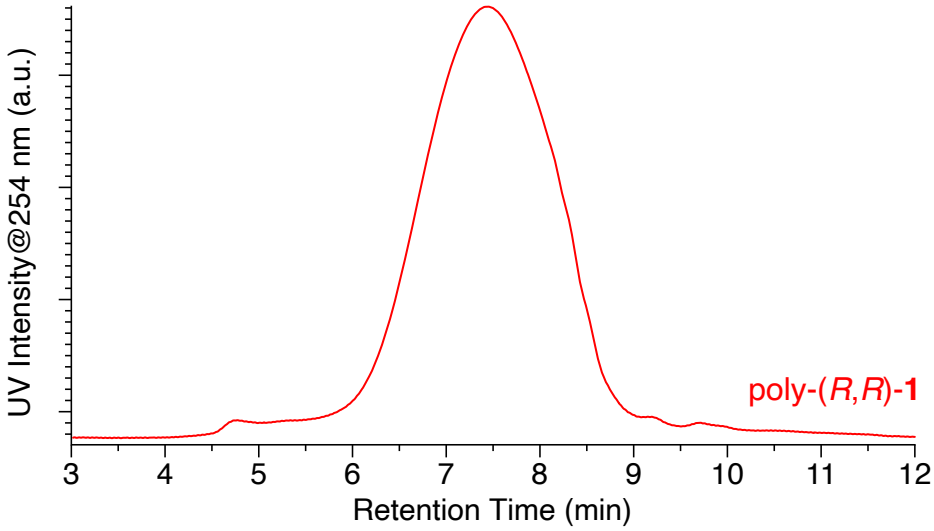

Fig. S47. SEC trace of poly-(*R*,*R*)-**1**.

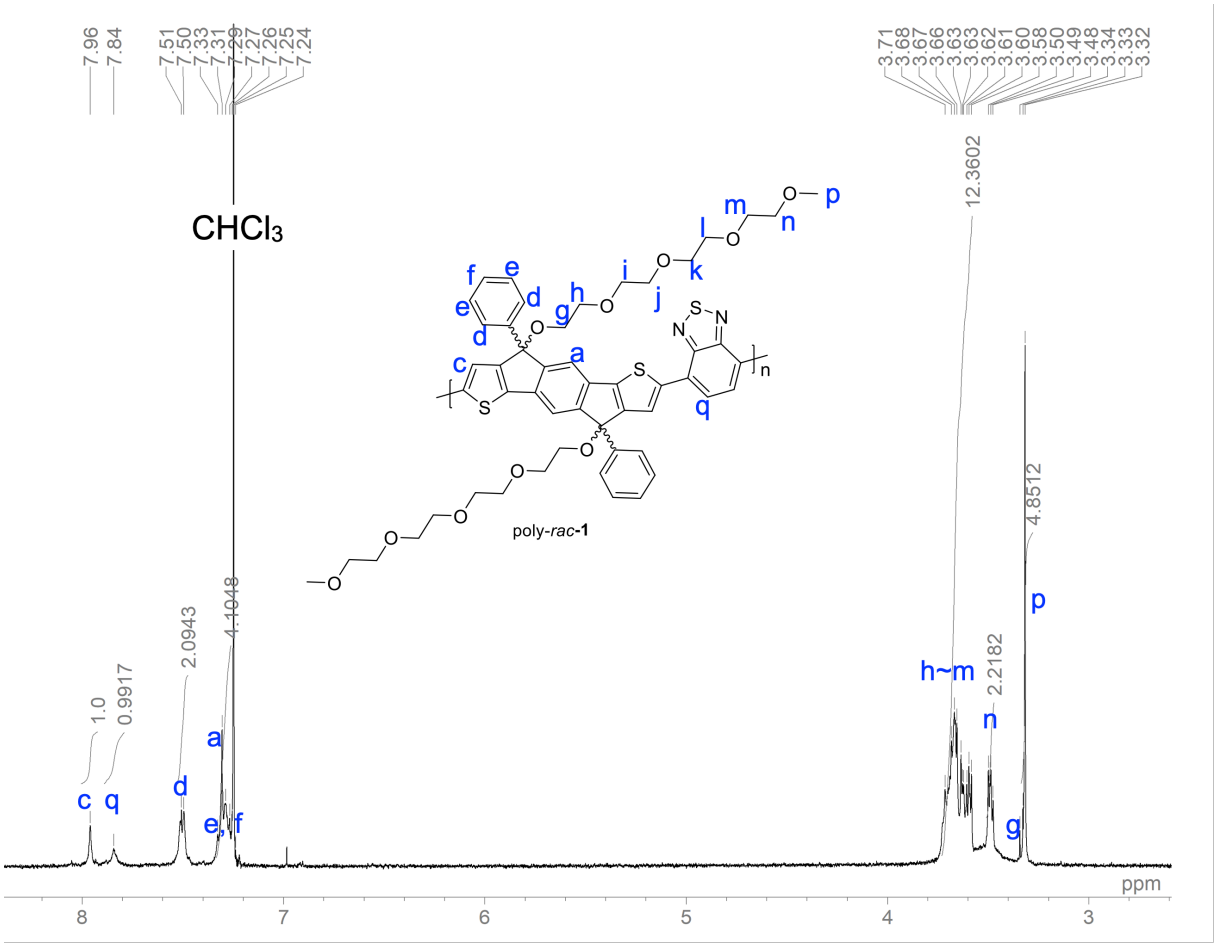

Fig. S48. ^{1}H NMR spectrum (400 MHz) of poly-*rac*-**1** in $CDCl_3$ at 25 °C.

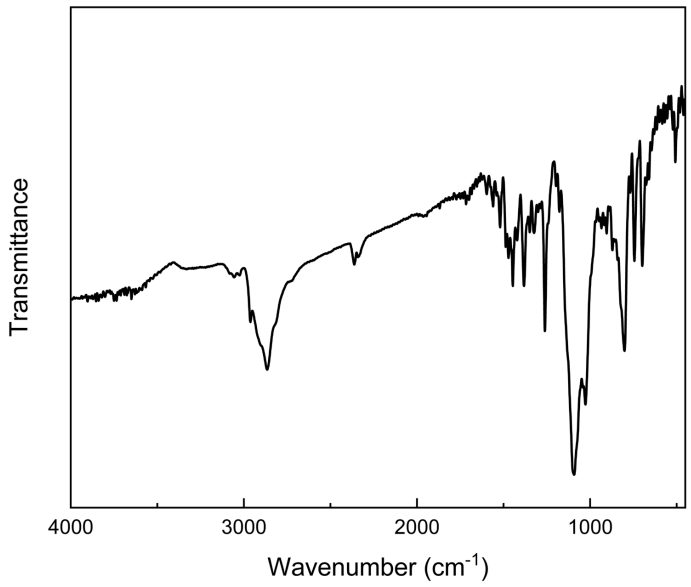

Fig. S49. FT-IR spectrum of poly-*rac*-**1** at 25 °C (KBr).

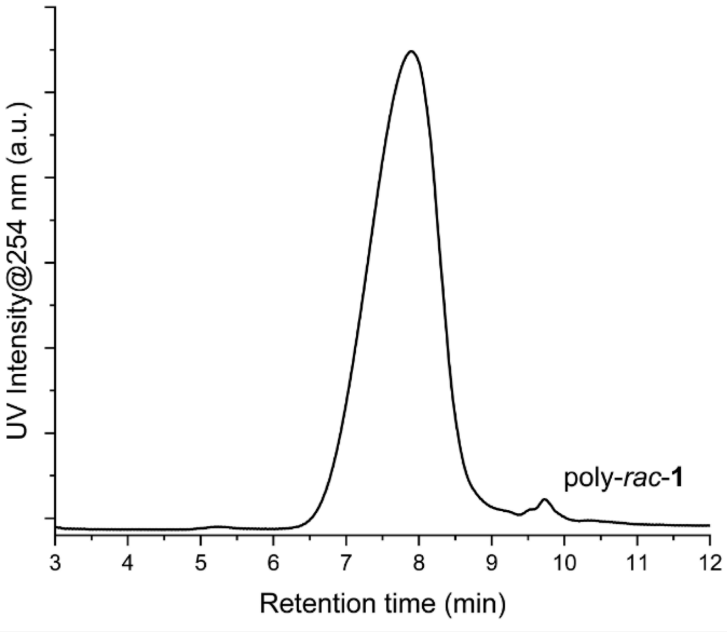

Fig. S50. SEC trace of poly-*rac*-**1**.

8. Supporting Tables

Table S1. Cartesian coordinates of the optimized geometry of (*S*,*S*)-**6** (a singlet state in vacuum) at the B3LYP/6-311G(d,p) level. Total energy is –2103.44423660 hartree.

C	0.85922	-1.07968	-0.58419
C	-0.51562	-1.33027	-0.57846
C	-1.364	-0.23689	-0.5732
C	-0.85922	1.07966	-0.58419
C	0.51562	1.33026	-0.57843
C	1.36399	0.23687	-0.57317
C	2.90692	0.23822	-0.59498
C	3.19401	-1.26428	-0.60829
C	2.01344	-1.96636	-0.60598
C	-2.90692	-0.23823	-0.59504
C	-3.194	1.26427	-0.60834
C	-2.01344	1.96634	-0.60599
C	4.34085	-2.10283	-0.57635
C	4.00213	-3.42961	-0.571
S	2.27347	-3.67446	-0.58668
C	-4.34084	2.10285	-0.57643
C	-4.00211	3.42961	-0.57106
S	-2.27344	3.67445	-0.58668
O	3.26746	0.91093	-1.80851
O	-3.26745	-0.91091	-1.80859
C	4.61503	0.76229	-2.23673
C	-4.61499	-0.76221	-2.23685
C	3.48084	0.96354	0.63213
C	-3.48086	-0.96355	0.63205
C	3.65562	0.3053	1.85361
C	4.11966	0.99453	2.97133
C	4.42171	2.35175	2.88506
C	4.25154	3.01515	1.67238
C	3.78189	2.32737	0.55558
C	-3.78173	-2.32743	0.55555
C	-4.25139	-3.01521	1.67235
C	-4.42174	-2.35176	2.88498
C	-4.11987	-0.99449	2.9712
C	-3.65583	-0.30527	1.85348
H	-0.90501	-2.34142	-0.57771
H	0.90501	2.3414	-0.57764
H	5.36586	-1.75944	-0.54744
H	4.65571	-4.28813	-0.56001
H	-5.36585	1.75943	-0.54755
H	-4.65568	4.28814	-0.56007
H	4.74123	1.44705	-3.07596
H	5.33064	1.02862	-1.44941
H	4.81573	-0.25797	-2.57974
H	-4.7412	-1.44696	-3.07609
H	-5.33064	-1.02852	-1.44955
H	-4.81564	0.25804	-2.5799
H	3.42606	-0.75066	1.93226
H	4.24812	0.46767	3.91045
H	4.78732	2.88659	3.75443
H	4.48415	4.07152	1.59317
H	3.65017	2.84351	-0.38729
H	-3.64987	-2.84361	-0.38728
H	-4.48386	-4.07161	1.59318
H	-4.78736	-2.8866	3.75435
H	-4.24848	-0.46762	3.91029
H	-3.4264	0.75072	1.9321

Table S2. Cartesian coordinates of the optimized geometry of (*R*,*R*)-**6** (a singlet state in vacuum) at the B3LYP/6-311G(d,p) level. Total energy is –2103.44423660 hartree.

C	-0.85922	-1.07968	-0.58419
C	0.51562	-1.33027	-0.57846
C	1.364	-0.23689	-0.5732
C	0.85922	1.07966	-0.58419
C	-0.51562	1.33026	-0.57843
C	-1.36399	0.23687	-0.57317
C	-2.90692	0.23822	-0.59498
C	-3.19401	-1.26428	-0.60829
C	-2.01344	-1.96636	-0.60598
C	2.90692	-0.23823	-0.59504
C	3.194	1.26427	-0.60834
C	2.01344	1.96634	-0.60599
C	-4.34085	-2.10283	-0.57635
C	-4.00213	-3.42961	-0.571
S	-2.27347	-3.67446	-0.58668
C	4.34084	2.10285	-0.57643
C	4.00211	3.42961	-0.57106
S	2.27344	3.67445	-0.58668
O	-3.26746	0.91093	-1.80851
O	3.26745	-0.91091	-1.80859
C	-4.61503	0.76229	-2.23673
C	4.61499	-0.76221	-2.23685
C	-3.48084	0.96354	0.63213
C	3.48086	-0.96355	0.63205
C	-3.65562	0.3053	1.85361
C	-4.11966	0.99453	2.97133
C	-4.42171	2.35175	2.88506
C	-4.25154	3.01515	1.67238
C	-3.78189	2.32737	0.55558
C	3.78173	-2.32743	0.55555
C	4.25139	-3.01521	1.67235
C	4.42174	-2.35176	2.88498
C	4.11987	-0.99449	2.9712
C	3.65583	-0.30527	1.85348
H	0.90501	-2.34142	-0.57771
H	-0.90501	2.3414	-0.57764
H	-5.36586	-1.75944	-0.54744
H	-4.65571	-4.28813	-0.56001
H	5.36585	1.75943	-0.54755
H	4.65568	4.28814	-0.56007
H	-4.74123	1.44705	-3.07596
H	-5.33064	1.02862	-1.44941
H	-4.81573	-0.25797	-2.57974
H	4.7412	-1.44696	-3.07609
H	5.33064	-1.02852	-1.44955
H	4.81564	0.25804	-2.5799
H	-3.42606	-0.75066	1.93226
H	-4.24812	0.46767	3.91045
H	-4.78732	2.88659	3.75443
H	-4.48415	4.07152	1.59317
H	-3.65017	2.84351	-0.38729
H	3.64987	-2.84361	-0.38728
H	4.48386	-4.07161	1.59318
H	4.78736	-2.8866	3.75435
H	4.24848	-0.46762	3.91029
H	3.4264	0.75072	1.9321

Table S3. Cartesian coordinates of the optimized geometry of (*S*,*S*)-**1** (a singlet state in vacuum) at the B3LYP/6-311G(d,p) level. Total energy is –7249.98948280 hartree.

C	1.27967	-0.49237	-0.47594
C	0.22967	-1.40288	-0.47109
C	-1.05054	-0.88999	-0.46443
C	-1.27963	0.49244	-0.47597
C	-0.22962	1.40295	-0.47115
C	1.05058	0.89005	-0.46447
C	2.37094	1.67234	-0.48489
C	3.3777	0.52777	-0.50282
C	2.72668	-0.66912	-0.49859
C	-2.37089	-1.67225	-0.48491
C	-3.37765	-0.52773	-0.50287
C	-2.72664	0.66918	-0.49865
C	4.79125	0.39977	-0.46466
C	5.15908	-0.90967	-0.4527
S	3.80786	-2.00493	-0.47006
C	-4.7912	-0.39974	-0.4647
C	-5.15905	0.9097	-0.45288
S	-3.80785	2.00497	-0.47025
O	2.34377	2.4377	-1.6813
O	-2.34364	-2.43759	-1.68136
C	3.57742	2.99125	-2.09597
C	-3.57725	-2.99117	-2.09607
C	2.49916	2.57274	0.74531
C	-2.49916	-2.57276	0.74524
C	2.97448	2.08218	1.95821
C	3.02588	2.89952	3.07772
C	2.60763	4.22013	2.9995
C	2.1336	4.71629	1.79409
C	2.07728	3.89743	0.67532
C	-2.0771	-3.8974	0.67523
C	-2.13355	-4.71636	1.79391
C	-2.60793	-4.22039	2.99927
C	-3.02633	-2.89983	3.07752
C	-2.97476	-2.08237	1.95811
Br	-6.91307	1.58007	-0.42431
Br	6.91309	-1.58005	-0.42436
H	0.40377	-2.47185	-0.47204
H	-0.40372	2.47192	-0.47211
H	5.50189	1.21217	-0.43628
H	-5.50183	-1.21214	-0.43615
H	3.34798	3.66684	-2.91875
H	4.06208	3.55928	-1.29429
H	4.25989	2.21633	-2.45659
H	-3.34776	-3.66686	-2.91876
H	-4.06199	-3.5591	-1.29437
H	-4.25969	-2.2163	-2.45686
H	3.30494	1.05326	2.03022
H	3.39803	2.50212	4.0145
H	2.65238	4.85912	3.87321
H	1.80519	5.74646	1.72203
H	1.70875	4.28298	-0.26667
H	-1.70844	-4.28289	-0.26674
H	-1.80502	-5.7465	1.72182
H	-2.65279	-4.85947	3.8729
H	-3.39868	-2.50254	4.01427
H	-3.30529	-1.05346	2.03015

Table S4. Cartesian coordinates of the optimized geometry of (*R*,*R*)-**1** (a singlet state in vacuum) at the B3LYP/6-311G(d,p) level. Total energy is –7249.98948583 hartree.

C	1.27972	0.49258	-0.47532
C	0.2297	1.40305	-0.47059
C	-1.05051	0.89012	-0.46417
C	-1.27953	-0.4923	-0.47572
C	-0.22949	-1.40279	-0.47077
C	1.05068	-0.88987	-0.46403
C	2.37108	-1.67208	-0.4845
C	3.37774	-0.52756	-0.50201
C	2.72675	0.66938	-0.49762
C	-2.37089	1.67234	-0.48474
C	-3.37758	0.52773	-0.50261
C	-2.72652	-0.66913	-0.49835
C	4.7913	-0.3996	-0.4643
C	5.15918	0.90983	-0.45274
S	3.8080	2.00509	-0.46964
C	-4.79112	0.39971	-0.4646
C	-5.15893	-0.90973	-0.45295
S	-3.80769	-2.00496	-0.47008
O	2.34392	-2.43712	-1.68124
O	-2.3437	2.43757	-1.68129
C	3.57752	-2.99053	-2.09617
C	-3.57737	2.9911	-2.09594
C	2.49897	-2.573	0.74538
C	-2.49925	2.57293	0.7453
C	2.97452	-2.08323	1.95849
C	3.0259	-2.90123	3.07748
C	2.6073	-4.2217	2.99855
C	2.13287	-4.71701	1.79297
C	2.07667	-3.89751	0.67466
C	-2.97479	2.08254	1.95818
C	-3.02649	2.90006	3.07753
C	-2.60828	4.22067	2.99919
C	-2.13394	4.71663	1.79382
C	-2.07736	3.89761	0.67519
Br	-6.91294	-1.58015	-0.42476
Br	6.91321	1.58019	-0.42465
H	0.40379	2.47202	-0.47139
H	-0.40358	-2.47176	-0.47182
H	5.50186	-1.21206	-0.43569
H	-5.50175	1.21212	-0.43616
H	3.34808	-3.66508	-2.91982
H	4.26038	-2.21548	-2.45575
H	4.06175	-3.55971	-1.29504
H	-3.34785	3.66769	-2.91789
H	-4.25938	2.2163	-2.45768
H	-4.06261	3.55812	-1.2939
H	3.30506	-1.05436	2.03103
H	3.39828	-2.50453	4.01448
H	2.65218	-4.8612	3.87187
H	1.80404	-5.74702	1.72041
H	1.7081	-4.28241	-0.26758
H	-3.30517	1.05359	2.03028
H	-3.39878	2.50278	4.01431
H	-2.65328	4.8598	3.87277
H	-1.80555	5.7468	1.72168
H	-1.70868	4.28302	-0.26679

9. Supporting References

S1. H. Zhang, M. Liu, W. Yang, L. Judin, T. I. Hukka, A. Priimagi, Z. Deng, P. Vivo, *ACS Adv. Mater. Interfaces* 2019, **6**, 1901036.

S2. N. Minoi, F. Ishiwari, K. Murotani, R. Nishikubo, T. Fukushima, A. Saeki, *ACS Appl. Mater. Interfaces* 2023, **15**, 6708–6715.

S3. M. J. Frisch, G. W. Trucks, H. B. Schlegel, G. E. Scuseria, M. A. Robb, J. R. Cheeseman, G. Scalmani, V. Barone, G. A. Petersson, H. Nakatsuji, X. Li, M. Caricato, A. V. Marenich, J. Bloino, B. G. Janesko, R. Gomperts, B. Mennucci, H. P. Hratchian, J. V. Ortiz, A. F. Izmaylov, J. L. Sonnenberg, D. Williams-Young, F. Ding, F. Lipparini, F. Egidi, J. Goings, B. Peng, A. Petrone, T. Henderson, D. Ranasinghe, V. G. Zakrzewski, J. Gao, N. Rega, G. Zheng, W. Liang, M. Hada, M. Ehara, K. Toyota, R. Fukuda, J. Hasegawa, M. Ishida, T. Nakajima, Y. Honda, O. Kitao, H. Nakai, T. Vreven, K. Throssell, J. A. Montgomery, Jr., J. E. Peralta, F. Ogliaro, M. J. Bearpark, J. J. Heyd, E. N. Brothers, K. N. Kudin, V. N. Staroverov, T. A. Keith, R. Kobayashi, J. Normand, K. Raghavachari, A. P. Rendell, J. C. Burant, S. S. Iyengar, J. Tomasi, M. Cossi, J. M. Millam, M. Klene, C. Adamo, R. Cammi, J. W. Ochterski, R. L. Martin, K. Morokuma, O. Farkas, J. B. Foresman and D. J. Fox, Gaussian, Inc., Gaussian 16, Revision B.01, Wallingford CT, **2016**.

S4. G. Albano, G. Pescitelli, L. Di Bari, *Chem*. *Rev*. 2020, **120**, 10145.